TXNDC5 Governs Extracellular Matrix Homeostasis in Pulmonary Hypertension

Zhen Chen[1*]; Fanhao Kong[1*]; Lixin Huang[1*]; Wenze Wu[1*]; Ziping Wang[1]; Hanbin Chen[1]; Junting Zhang[1]; Lin Deng[6]; Chengrui Cao[1]; Xiaoyan Zhang[1]; Zixin Liu[2]; Kai-Chien Yang[3#]; Wei-Ting Chang[4, 5#]; Jin-Song Bian[1#]; Xiaowei Nie[2#];

1 Department of Pharmacology, Joint Laboratory of Guangdong-Hong Kong Universities for Vascular Homeostasis and Diseases, SUSTech Homeostatic Medicine Institute, School of Medicine, Southern University of Science and Technology, Shenzhen 518055, China.

2 Department of Human Cell Biology and Genetics, SUSTech Homeostatic Medicine Institute, School of Medicine, Southern University of Science and Technology, Shenzhen 518055, China.

3 Department and Graduate Institute of Pharmacology, National Taiwan University College of Medicine, Taipei, Taiwan

4 School of Medicine, College of Medicine, National Sun Yat-sen University, Kaohsiung, Taiwan

5 Division of Cardiology, Department of Internal Medicine, Chi Mei Medical Center, Tainan

6 Department of Cardiology, The Eighth Affiliated Hospital, Sun Yat-sen University, Shenzhen, China

[*]These authors contributed equally to this work.

[#]Correspondence to:

Xiaowei Nie, PhD, E-mail niexw@sustech.edu.cn.

Jin-Song Bian, PhD, E-mail bianjs@sustech.edu.cn.

Wei-Ting Chang, PhD, E-mail cmcvecho2@gmail.com.

Kai-Chien Yang, PhD, E-mail allenmy0920@gmail.com.

ABSTRACT

BACKGROUND: Pulmonary hypertension (PH) is characterized by vascular remodeling without effective treatments. The initiation and progression of PH are heavily influenced by the dysfunction of pulmonary artery endothelial cells. Thioredoxin domain containing 5 (TXNDC5), a member of the protein disulfide isomerases (PDI) family, catalyzes the formation and rearrangement of disulfide bonds in proteins, crucial for endothelial cell function and maintaining vascular homeostasis in cardiovascular diseases, yet its role in PH remains unclear.

METHODS: Label-free proteomics was used to reveal the PDI protein expression profile in hypoxic PH patients. Multiplex immunofluorescence and Western blot analyses were performed to investigate the pathological role of TXNDC5. Mice with adeno-associated virus-mediated lung endothelial TXNDC5 overexpression, global knockout, and endothelial ablation of TXNDC5 were used to study the role of TXNDC5 in rodent PH models. *In vitro* experiments with cultured pulmonary arterial endothelial cells and bioinformatics assays were used to elucidate the underlying mechanisms. Pharmacological inhibition and endothelial-targeted TXNDC5 gene therapy were evaluated for their effects in PH.

RESULTS: TXNDC5 was significantly upregulated in the lungs of both PH patients and rodent models, with prominent expression in the endothelial layer of remodeled distal pulmonary arteries. Overexpression of TXNDC5 exacerbated Sugen5416/hypoxia (SuHx)-induced pulmonary artery remodeling, increased right ventricular systolic pressure, and right ventricular hypertrophy. Global or endothelial-specific deficiency of TXNDC5 exerted protective efficacy against the SuHx challenge. RNA sequencing and protein-protein interaction analysis revealed TXNDC5 as a potential regulator of extracellular matrix (ECM) homeostasis, with biglycan (BGN) identified as a critical downstream effector. TXNDC5 required BGN to regulate the ubiquitination of HIF-1α/2α, resulting in its abnormal accumulation to drive PH development. E64FC26, a TXNDC5 inhibitor, and endothelial-targeted TXNDC5 gene therapy exhibited therapeutic efficacy in SuHx-induced PH rats.

CONCLUSIONS: Our study reveals that TXNDC5 is a main modulator to regulate ECM homeostasis and may serve as a promising target for the treatment of PH.

Key Words: pulmonary hypertension**,** extracellular matrix, TXNDC5, BGN, HIF signaling

INTRODUCTION

Pulmonary hypertension (PH) is a serious cardiovascular disease characterized by elevated pulmonary artery pressure and right heart failure, with high morbidity and mortality[1]. Hypoxia is a significant trigger for PH, with hypoxia-induced and/or lung disease-related PH (Group III) being one of the most common types clinically[2]. Hypoxia-induced dysfunction in pulmonary artery endothelial cells (PAECs) initiates pulmonary vasoconstriction[3]. Subsequently, pulmonary artery smooth muscle cells (PASMCs) switch to a hyperproliferative and apoptosis-resistant phenotype, leading to vascular remodeling[4]. However, there remains no curative clinical treatment option for reversing remodeled vessels against the disease[5,6]. It highlights the need for further exploration of PH pathogenesis and new therapeutic targets.

Protein disulfide isomerase (PDI) is a family of enzymes located in the endoplasmic reticulum that facilitates the disulfide bond formation and rearrangement, aiding protein proper folding[7,8]. This family comprises 21 members, each containing thioredoxin-like domains involved in redox reactions, particularly under hypoxic conditions[9]. PDI proteins are implicated in the modulation of endothelial cell function to maintain vascular homeostasis. PDIA1 regulated the expression and redox state of hypoxia-inducible factor (HIF)-1α by promoting its lysosomal degradation by influencing the formation of disulfide bonds[10]. It also enhances vascular endothelial growth factor receptor 2 (VEGFR2) signaling, thereby promoting endothelial cell migration, proliferation, and angiogenic responses[11]. As a member of the PDI family, TXNDC5 is mainly expressed in endothelial cells (ECs) and is also known as endothelial PDI (Endo-PDI). Its abnormal expression is associated with multiple

disorders such as organ fibrosis[12], diabetes[13], rheumatoid arthritis[14], and cancers[15]. Additionally, inhibition of TXNDC5 restores endothelial dysfunction to mitigate vascular calcification and atherosclerosis[16,17]. However, the role of PDI proteins in pulmonary vascular remodeling in PH remains unclear.

Extracellular matrix (ECM) is a complex network of proteins and polysaccharides secreted by cells, providing structural and communicative support to adjacent cells[18]. Remodeling of pulmonary arterial ECM occurs in the early stage of PH pathogenesis, before increased wall thickness and pulmonary artery pressure. ECM remodeling is the cause rather than a consequence of pulmonary vascular remodeling in PH[19]. Recently, we revealed that the ECM proteins in PAECs accelerated pulmonary vascular remodeling through interaction with HIF-1α in a positive feedback loop manner, providing evidence for early intervention in ECM remodeling to prevent PH progression[20,21].

In this study, we performed 4D label-free proteomics to reveal the expression profile of PDI proteins from the lungs of patients with hypoxic PH. We found that TXNDC5 was one of the most significantly upregulated proteins. Global or endothelial cell-specific deficiency of TXNDC5 alleviated Sugen5416/hypoxia (SuHx)-induced PH, whereas TXNDC5 overexpression aggravated PH. Importantly, the silencing of TXNDC5 preserved ECM homeostasis to alleviate PA remodeling and restore endothelial function. In addition, TXNDC5 directly interacted with biglycan (BGN) and assisted its protein folding to drive PH development. Furthermore, TXNDC5 required BGN to regulate the HIF-1α/2α ubiquitination, resulting in its abnormal aggregation. Importantly, pharmacological inhibition of TXNDC5 with E64FC26 or pulmonary endothelium-targeted TXNDC5 silencing effectively mitigated PH in rats. The present study therefore demonstrated for the first time that TXNDC5 may be a key protein to control ECM homeostasis and a promising therapeutic target for PH.

METHODS

Detailed expanded methods and materials are available in **Supplemental Material 1**.

Study Approval

All human samples were obtained from the Shenzhen People's Hospital (China) and Wuxi People's Hospital (China) with the informed consent of the patients, which was approved by the Ethics Committee for the Use of Human Subjects following The Code of Ethics of the Helsinki Declaration of the World Medical Association. All animal studies followed the guidelines of the Committee on Animal Research and Ethics of the Southern University of Science and Technology (China).

Data Availability Statement

Source data and original blots or gel images for this study are available from the corresponding author upon reasonable request.

Statistical Analysis

Data were analyzed with GraphPad Prism 8.0 software and were expressed as the mean±standard deviation (mean±SD). For comparisons between two groups with a normal distribution, an unpaired 2-tailed Student *t*-test was performed. When the data did not follow a normal distribution, the non-parametric Mann-Whitney U test was applied. For data involving more than two groups, one-way ANOVA was used, followed by Tukey's honestly significant difference test for multiple comparisons. For two variables, two-way ANOVA with Tukey's honestly significant difference test for multiple comparisons was applied. Statistical significance was defined as $P<0.05$.

RESULTS

TXNDC5 Expression is Increased in PH Patients and Rodent Models

We performed 4D label-free proteomics on lung samples from 5 patients with hypoxic PH and 5 non-PH donors (**Figure S1A**). Among the human PDI family proteins, TXNDC5 was the most markedly dysregulated member in PH patients compared with donors (fold change=3.45, P=0.0048) (**Figure 1A**). The involvement of TXNDC5 in PH was then confirmed by assessing its protein and mRNA expressions in the lungs of

147 PH patients as compared with non-PH donors (**Figure 1B-C**). Western blotting further
148 showed that TXNDC5 expression was also significantly increased in multiple rat PH
149 models and mouse PH models compared with controls (**Figure 1D** and **Figure S1B**).
150 In distal pulmonary arteries (PAs), multiplex immunofluorescence (mIF) assays
151 demonstrated pronounced co-localization of TXNDC5 with the endothelial marker
152 CD31. By contrast, co-localization of TXNDC5 with α-SMA (a marker for smooth
153 muscle cells) and COL1A1 (a marker for fibroblasts) was marginal (**Figure 1E-G** and
154 **Figure S1C**). Furthermore, TXNDC5 expression was significantly elevated in the
155 $CD31^{+}$ intima of severely remodeled PAs from patients with interstitial lung disease
156 (ILD)-PH and chronic obstructive pulmonary disease (COPD)-PH patients, compared
157 with non-PH donors (**Figure 1H**). Similar results were observed in the remodeled PAs
158 of SuHx- or monocrotaline (MCT)-induced PH rat models, indicating that TXNDC5
159 upregulation is a conserved feature of pulmonary artery (PA) remodeling (**Figure 1I-K**
160 and **Figure S1D**). Moreover, Western blot analysis of primary lung ECs isolated from
161 PH rodent models confirmed the TXNDC5 upregulation (**Figure S1E-F**). Notably,
162 correlations between intimal TXNDC5 mean fluorescence intensity (MFI) and PH
163 severity were observed in rats, with positive correlations with right ventricular systolic
164 pressure (RVSP) and Fulton index (right ventricle weight to left ventricle plus
165 interventricular septum weight, ie, RV/(LV+S)), and a negative correlation with
166 tricuspid annular plane systolic excursion (TAPSE) (**Figure 1L-N**). Taken together,
167 these findings suggest that the TXNDC5 may be a critical dysregulated factor in ECs
168 within the pulmonary vasculature that contributes to PH pathogenesis.
169

170 **TXNDC5 Mediates the Development of SuHx-Induced PH**

171 To investigate the role of TXNDC5 *in vivo* in the development of experimental
172 PH, we created TXNDC5 knockout ($TXNDC5^{-/-}$) mice, which were then challenged
173 with or without SuHx (**Figure 2A**). We found that deletion of TXNDC5 alone had no
174 significant effects but markedly reduced both RVSP (**Figure 2B**) and RV/(LV+S)
175 (**Figure S2A**) in male mice. Echocardiography analysis also showed that TXNDC5
176 deficiency significantly improved the right ventricular (RV) function, as indicated by

177 increased PA acceleration time/ PA ejection time ratio (PAT/PET), TAPSE, and right
178 ventricular fractional area change (RVFAC) (**Figure S2B-D**), along with reduced right
179 ventricular free wall thickness (RVFWT) (**Figure S2E**). In addition, using mIF and
180 Victoria blue/Sirius red (VB/SR) staining, we evaluated distal PA remodeling in mice
181 (**Figure 2C**). Under normal conditions, no significant abnormal histological change
182 was found in TXNDC5$^{-/-}$ mice compared with wild-type (WT) littermates. Notably,
183 TXNDC5 deficiency markedly reduced PA muscularization, decreased medial wall
184 thickness, and diminished collagen deposition area compared with WT littermates
185 (**Figure 2D-F**). Consistent with the PA changes, wheat germ agglutinin (WGA) staining
186 also proved that the RV cardiomyocyte hypertrophy was markedly inhibited in SuHx-
187 treated TXNDC5$^{-/-}$ mice when compared with their control littermates (**Figure 2G**).
188 Notably, these protective effects of TXNDC5 deficiency were also confirmed in female
189 mice. In SuHx-treated female TXNDC5$^{-/-}$ mice, we observed similar reductions in
190 RVSP and RV/(LV+S) (**Figure S2F-G**), improvements in echocardiographic
191 parameters (**Figure S2H-K**), as well as attenuated distal PA remodeling compared with
192 female WT controls (**Figure S2L-O**). These data indicate that TXNDC5 deletion
193 protects against SuHx-induced PH.

194 With a gain-of-function approach, we next examined whether overexpression of
195 TXNDC5 can influence the development of PH in SuHx-treated mice. TXNDC5 was
196 exogenously delivered via tail vein injection using an adeno-associated virus serotype
197 engineered to specifically target lung endothelial cells (AAV-TXN) (**Figure 2H**). *Ex*
198 *vivo* imaging of various organs confirmed that preferential accumulation of AAV-TXN
199 in the lungs (**Figure 2I**). Consistently, co-immunofluorescence staining further
200 demonstrated strong colocalization of GFP-TXNDC5 with anti-CD31 in pulmonary
201 arteries (**Figure S2P**). Furthermore, Western blot analysis of primary lung ECs further
202 verified the EC-specific TXNDC5 overexpression (**Figure S2Q**). Hemodynamic
203 measurement revealed that both male and female mice administered with AAV-TXN
204 increased the RVSP compared with those administered with control AAV (AAV-NC)
205 even under normoxic conditions. In response to the SuHx challenge, AAV-TXN mice
206 further increased in both RVSP and RV/(LV+S) compared with AAV-NC mice (**Figure**

207 **2J** and **Figure S2R**). Echocardiography analysis also showed that AAV-TXN reduced
208 PAT/PET, TAPSE RVFAC, and increased RVFWT compared with AAV-NC mice under
209 SuHx, although no significant differences were observed under normoxic conditions
210 (**Figure S2S-V**). In addition, mIF and VB/SR staining confirmed exacerbated
211 remodeling of distal PAs in AAV-TXN mice compared with AAV-NC mice upon SuHx
212 treatment, as indicated by increased PA muscularization, medial wall thickness, and
213 collagen deposition area (**Figure 2K-N**). Conversely, endothelial TXNDC5
214 overexpression was found to exacerbate SuHx-induced PH.
215
216 **Endothelial Cell-Specific Deletion of TXNDC5 Ameliorates SuHx-Induced PH**
217 To examine the role of endothelial TXNDC5 in the development of PH, we
218 generated endothelial cell-specific TXNDC5 knockout mice ($TXNDC5^{ECKO}$) (**Figure**
219 **3A** and **Figure S3A**) and validated them with Western blots (**Figure S3B**). SuHx-
220 induced RVSP and RV/(LV+S) elevation (**Figure 3B-C**), as well as impaired RV
221 function (**Figure S3C-F**), were significantly improved by the deletion of endothelial
222 TXNDC5. The morphology of PAs in normoxic $TXNDC5^{ECKO}$ mice did not differ from
223 that of control littermates ($TXNDC5^{f/f}$ mice) under normoxia. In line with the
224 hemodynamic and echocardiographic changes, $TXNDC5^{ECKO}$ mice exhibited reduced
225 muscularized PAs, medial wall thickness, and collagen deposition induced by SuHx
226 compared with $TXNDC5^{f/f}$ mice (**Figure 3D-G**). Using a standardized lung
227 angiography, we confirmed that SuHx treatment led to distal PA remodeling, manifested
228 as restricted intrapulmonary contrast agent distribution in $TXNDC5^{f/f}$ mice. In contrast,
229 $TXNDC5^{ECKO}$ mice displayed markedly improved angiographic filling, indicative of
230 better-preserved pulmonary vasculature (**Figure 3H** and **Figure S3G**). In addition to
231 vascular changes, SuHx-induced RV hypertrophy was also markedly attenuated in
232 $TXNDC5^{ECKO}$ mice, as evidenced by reduced RV wall thickness and decreased
233 cardiomyocyte cross-sectional area (**Figure 3I-J**). Importantly, comparable protective
234 effects were also observed in female $TXNDC5^{ECKO}$ mice, as evidenced by reduced
235 RVSP and RV hypertrophy (**Figure S3H-I**), improved RV function on
236 echocardiography (**Figure S3J-M**), and attenuated distal PA remodeling (**Figure S3N-**

Q). Together, these findings demonstrate that endothelial cell-specific deletion of TXNDC5 ameliorates SuHx-induced PH in mice, with consistent benefits across sexes. These data underscore the crucial role of endothelial TXNDC5 in the development of PH and highlight its potential as a sex-independent therapeutic target.

TXNDC5 Promotes Hypoxia-Induced Dysfunction in Pulmonary Arterial Cells

Exposure to hypoxia significantly increased the protein and mRNA levels of TXNDC5 in hPAECs (**Figure S4A-B**). Immunofluorescent staining further confirmed that TXNDC5 expression was upregulated upon hypoxia treatment and was mainly located in the cytoplasm (**Figure S4C**). Targeting TXNDC5 small-interfering RNA oligonucleotides (siTXNDC5) was used to silence TXNDC5 expression in hPAECs. EdU staining showed that knocking down TXNDC5 expression suppressed the proliferation of hPAECs under both normoxic and hypoxic conditions (**Figure S4D**). In addition, siTXNDC5 treatment also abated the hypoxia-induced migration ability of hPAECs (**Figure S4E**). To further evaluate the role of increased TXNDC5 in hPAECs, we overexpressed TXNDC5 in hPAECs by transducing with lentivirus (LV-TXNDC5). TXNDC5 overexpression visibly altered cytoskeletal architecture, which displayed prominent stress fibers and a more diffuse pattern of paxillin distribution (**Figure S4F-G**). Furthermore, flow cytometry showed that the silencing of TXNDC5 prevented the G1 to S phase transition (**Figure S4H**) of hPAECs under both normoxic and hypoxic conditions. Taken together, TXNDC5 regulates many important functional abnormalities associated with PH pathogenesis, with disruption of cytoskeletal architecture in hPAECs.

The hyper-proliferation and resistance to apoptosis of PASMCs directly accelerate the remodeling of PAs in PH[22]. Thus, we also investigated whether endothelial TXNDC5 affects the function of hPASMCs via influencing paracrine patterns. For this purpose, hPAECs were transfected with siTXNDC5 under hypoxia or normoxia conditions, and their conditioned medium (siTXN-CM) was collected to treat hPASMCs. Assessment of cell proliferation showed that siTXN-CM significantly downregulated cyclin A and proliferating cell nuclear antigen (PCNA) expression under

both normoxic and hypoxic conditions (**Figure S4I**). Consistently, EdU incorporation assays further confirmed that siTXN-CM suppressed the proliferation of hPASMCs (**Figure S5A**). Cell Counting Kit-8 (CCK-8) assays further demonstrated that siTXN-CM decreased the viability of hPASMCs (**Figure S5B**). In addition, siTXN-CM enhanced hPASMCs apoptosis, as indicated by increased cleaved caspase-3 expression (**Figure S4J**). Collectively, our data demonstrate that hPAECs TXNDC5 plays a critical role in promoting hPASMCs proliferation, survival, and resistance to apoptosis.

TXNDC5 Regulates ECM Expression and Homeostasis

To explore the underlying downstream molecular mechanisms of TXNDC5, we performed a bulk RNA sequencing (RNA-seq) analysis on hPAECs transfected with siRNA targeting TXNDC5 under hypoxia exposure. Gene ontology analysis indicated that the silencing of TXNDC5 resulted in altered expression of genes mainly enriched in “collagen-containing ECM”, “ECM”, “ECM organization”, “ECM structural constituent”, “response to hypoxia”, and “cellular response to hypoxia” (**Figure 4A**). We selected the differentially expressed ECM genes and then constructed a protein-protein interaction (PPI) network (**Figure 4B**). The network revealed that TXNDC5-affected ECM proteins were clustered into different functional subgroups, including “proteoglycans and glycoproteins”, “collagens”, “matrix modulators and adhesion”, “metallopeptidase activity”, “basement membrane”, “growth factors and signaling regulators”, and “angiogenesis”. Immunofluorescence staining confirmed that periostin (POSTN), biglycan (BGN), lysyl oxidase (LOX), and transglutaminase 2 (TGM2) were excessively deposited in the PAs from $TXNDC5^{f/f}$ mice but not in $TXNDC5^{ECKO}$ mice under SuHx conditions (**Figure 4C-F** and **Figure S5C**). Western blot analysis also confirmed that TXNDC5 silencing reversed the abnormal expression of ECM proteins (COL1A1, TGM2, FN1, POSTN, LOX) induced by hypoxia treatment in hPAECs (**Figure 4G**).

To further investigate whether TXNDC5 regulates ECM secretion, we collected the supernatants from hPAECs. Dot blot analysis revealed that the silence of TXNDC5 markedly reduced the secretion of BGN, POSTN, and LOX **(Figure S5D-G)**. These

results provide a mechanistic explanation for why the conditional medium from TXNDC5-silenced hPAECs suppresses proliferation and viability while promoting apoptosis of hPASMCs. Collectively, these data highlight the key role TXNDC5 played in regulating ECM homeostasis.

BGN Is a Promising Biomarker and Therapeutic Target for Hypoxic Pulmonary Hypertension

We further explore the key TXNDC5-targeted ECM proteins that are responsible for the biological function of ECs. We performed a computational analysis of the PPI network between the ECM proteins dataset and the ECs function-related proteins dataset. By combining these two datasets, we constructed a huge original PPI network. A core network was finally obtained by progressively simplifying through degree values (**Figure 5A**). Through the intersection of 3 ECM datasets, core ECM in the above PPI network, TXNDC5 silencing in hPAECs, and hypoxia-treated hPAECs (GSE160255), we finally identified biglycan (BGN) (**Figure S5H**).

We first examined the level of BGN in lung biopsies from patients with hypoxic PH or healthy donors. Protein levels of BGN were increased in the lungs of PH patients as compared with non-PH donors (**Figure S5I**). A recently published GEO dataset (GSE254617) also showed markedly upregulated mRNA levels of BGN in the lungs of patients with idiopathic pulmonary arterial hypertension (IPAH) (**Figure 5B**). Consistent with human specimens, protein levels of BGN were also increased in rodent PH models, including SuHx-treated mice and rats and MCT-treated rats, as compared with controls (**Figure S5J-K**). We also investigated whether BGN can reflect the severity of PH by analyzing BGN levels in serum. Surprisingly, a markedly increased BGN level was found in the serum of 27 patients with hypoxic PH compared with the serum of 27 non-PH donors (**Figure 5C**). Additionally, BGN expression in serum exhibited a significant correlation with systolic pulmonary artery pressure (sPAP) (**Figure 5D**), suggesting that BGN may serve as a biomarker associated with PH. As a secreted protein, we further investigated the biological function of circulating BGN *in vitro*. EdU staining showed that treatment with recombinant human BGN (rhBGN)

327 significantly enhanced the proliferative capacity of hPASMCs compared with the
328 negative control (bovine serum albumin, BSA) (**Figure S5L**). Consistently, CCK-8
329 assays demonstrated increased cell viability following rhBGN treatment (**Figure S5M**).
330 In parallel, rhBGN induced an apoptosis-resistant phenotype in hPASMCs, as
331 evidenced by reduced cleaved caspase-3 expression (**Figure S5N**) and decreased
332 apoptotic cell populations detected by flow cytometry (**Figure S5O**).

333 To evaluate the specific role of BGN in PH generation, we then developed an
334 endothelial cell-specific BGN knockout mouse (BGN^{ECKO}) (**Figure S6A**), and the
335 absence of BGN in lung ECs was validated (**Figure S6B**). As BGN is an X
336 chromosome-located gene, male mice carry a single floxed allele ($BGN^{f/0}$), whereas
337 female mice carry double floxed alleles ($BGN^{f/f}$). Firstly, RVSP and RV/(LV+S) were
338 elevated in male mice with SuHx treatment, while endothelial cell-specific BGN
339 ablation ameliorated these compared with their control littermates ($BGN^{f/0}$) (**Figure**
340 **5E-F**). Consistent with changes in hemodynamics, BGN^{ECKO} mice showed abrogated
341 PAs remodeling, as shown by the mIF and VB/SR staining (**Figure 5G-I** and **Figure**
342 **S6C**). Lung angiogram also revealed the better-preserved lung vasculature in BGN^{ECKO}
343 mice, further indicating that endothelial BGN deletion effectively protects against distal
344 PA remodeling (**Figure 5J**). Histological assessment of the RV also revealed an increase
345 in RV wall thickness in the SuHx-$BGN^{f/0}$ group, which was significantly reduced in
346 BGN^{ECKO} mice treated with SuHx (**Figure 5K**). Moreover, echocardiography analysis
347 also showed that SuHx-induced reductions in PAT/PET, TAPSE, RVFAC, and increases
348 in RVFWT were greater in $BGN^{f/0}$ mice than in BGN^{ECKO} mice (**Figure S6D-G**).
349 Notably, similar protective effects were observed in female BGN^{ECKO} mice, with
350 comparable improvements in RVSP (**Figure S6H**), RV hypertrophy and function
351 (**Figure S6I-M**), and distal PA pathological remodeling compared with $BGN^{f/f}$ female
352 littermates (**Figure S6N-Q**). Together, our data suggest that endothelial BGN plays an
353 important role in PH development.

354

355 **TXNDC5 Assists BGN Protein Folding to Drive Pulmonary Hypertension**

356 To elucidate how TXNDC5 regulates BGN, we first performed Western blots to

validate the positive regulation of TXNDC5 on BGN both *in vitro* and *in vivo*. The silencing of TXNDC5 reversed the overexpression of BGN induced by hypoxia stimulation in hPAECs (**Figure S7A**). Reduced BGN expression was also observed in the lungs of TXNDC5-deficient mice (**Figure S7B**), which was consistent with the findings in primary lung ECs isolated from $TXNDC5^{ECKO}$ mice (**Figure S7C**). In contrast, BGN expression was elevated in hPAECs following lentiviral-mediated TXNDC5 overexpression (**Figure S7D**) and in primary lung ECs isolated from AAV-TXN-treated mice (**Figure S7E**).

To further assess the direct interaction between TXNDC5 and BGN, we investigated the subcellular location at which TXNDC5 binds to BGN. Immunostaining assays showed that TXNDC5 colocalized with BGN (**Figure 6A**). We also performed co-IP analysis and found that TXNDC5 bound to BGN, and the binding was enhanced upon hypoxia exposure (**Figure 6B** and **Figure S7F**). To identify the protein domain of TXNDC5 that was involved in the interaction with BGN, we performed molecular docking analysis and revealed that multiple sites of TXNDC5 (Cys89, Ser125, Gly351, and His352) might be involved in the interaction with BGN (**Figure 6C**). Thus, we constructed four TXNDC5 mutants (C89A, S125A, G351A, and H352A) to identify the residue that plays a key role in this process. Co-IP analysis showed that C89A and G351A could partially abolish TXNDC5 binding with BGN (**Figure 6D**), suggesting that these amino acid residues might be essential for the binding of TXNDC5 and BGN.

As an endoplasmic reticulum resident protein with 3 thioredoxin domains, TXNDC5 catalyzes the formation or rearrangement of substrate disulfide bonds. Each thioredoxin domain contains a highly conserved CGHC motif, which serves as the active site for PDI activity[15]. Thus, we hypothesized that TXNDC5 functions to facilitate the folding of BGN, allowing it to mature and subsequently exert signaling transduction and travel through the secretory pathway. To confirm the requirement for the PDI activity of TXNDC5 in assisting BGN folding, we generated a TXNDC5 mutant (TXNDC5 Mut) that lacks PDI activity by introducing cysteine-to-alanine mutations in each of its 3 thioredoxin domains (**Figure S7G**). As described previously[23], the extent of BGN protein folding can be examined using a fluorescence resonance

energy transfer (FRET)-based protein folding assay (**Figure S7H**). Application of a standard acceptor photobleaching FRET protocol in hPAECs revealed that LV-TXNDC5 significantly increased FRET efficiency while TXNDC5 Mut overexpression did not, suggesting that TXNDC5 assists BGN protein folding dependent on its PDI activity in hPAECs (**Figure 6E**). Moreover, a cycloheximide (CHX) protein chase assay was conducted to evaluate the stability of BGN in hPAECs. Overexpression of TXNDC5 markedly prolonged the half-life of BGN protein compared with LV-NC (**Figure S7I**), whereas TXNDC5 silencing accelerated BGN degradation, exerting the opposite effect (**Figure S7J**). Taken together, these results indicate that TXNDC5 depends on its PDI activity to contribute to the proper folding of BGN, maintaining its protein stability and subsequently secreting extracellular from hPAECs.

To assess whether BGN mediates the pathogenic effects of endothelial TXNDC5 *in vivo*, we performed a rescue experiment in endothelial BGN-deficient mice by specifically overexpressing TXNDC5 in lung ECs (**Figure 6F**). As shown by mIF and VB/SR staining, AAV-TXN exacerbated distal PA muscularization, medial wall thickness, and collagen deposition in $BGN^{f/f(f/0)}$ mice under SuHx conditions, whereas these effects were largely abolished in BGN^{ECKO} mice (**Figure 6G-J**). Consistently, AAV-TXN markedly increased RVSP (**Figure 6K**) and also aggravated RV hypertrophy in $BGN^{f/f(f/0)}$ mice, whereas both changes were significantly attenuated in BGN^{ECKO} mice (**Figure 6L**). Furthermore, echocardiographic assessment revealed that AAV-TXN led to pronounced deterioration of RV performance, as reflected by reduced PAT/PET, TAPSE, RVFAC, and elevated RVFWT. In contrast, these adverse functional changes were largely blunted in BGN^{ECKO} mice (**Figure S7K-N**). Together, these results indicate that endothelial BGN is required for TXNDC5-mediated pulmonary vascular remodeling and PH development, confirming BGN as a key downstream effector of TXNDC5.

A Positive Feedback Loop Exists Between TXNDC5 and HIF Signaling

Given that the HIF α subunits are the dominant effector activated by hypoxia, we hypothesize that HIF signaling regulates the transcription of TXNDC5. qPCR analysis

showed that silencing of HIF-2α, but not HIF-1α, markedly downregulated TXNDC5 mRNA levels under both normoxia and hypoxia conditions (**Figure S8A-B**). Western blot analysis also demonstrated that the protein level of TXNDC5 was significantly decreased when HIF-2α was knocked down (**Figure S8C**). Next, we identified two putative HIF-2α binding sites (BS) in the TXNDC5 promoter region by utilizing the available transcriptional factors database (hTFtarget and AnimalTFDB 4.0) (**Figure S8D**). To study how HIF-2α transcriptionally regulates TXNDC5, we performed a chromatin immunoprecipitation (ChIP) assay to examine whether HIF-2α binds to these BS. We designed primers that span the sequence from two BS to amplify from HIF-2α ChIP samples. Gel electrophoresis results showed that both primers could be amplified, indicating that HIF-2α binds to these regions of the TXNDC5 promoter (**Figure S8E**). Dual-luciferase reporter assays further revealed that mutation of each putative HIF-2α binding site within the TXNDC5 promoter individually reduced luciferase activity compared with the wild-type construct. Mutation of both sites caused a further decrease (**Figure 7A**). These results indicate that both BS1 and BS2 contribute synergistically to HIF-2α-mediated transcriptional activation of TXNDC5.

Following validation, we found that the HIF-1α/2α protein levels were significantly decreased by silencing of TXNDC5 under the hypoxic situation (**Figure S8F**), and similar results were also observed in the lungs of TXNDC5-deficient mice (**Figure 7B**). We also examined the nuclear localization of HIF-1α/2α. Western blot analysis and immunofluorescence staining consistently confirmed that TXNDC5 silencing decreased HIF-1α/2α levels in the nucleus under hypoxia exposure (**Figure S8G-H**). Together, these results suggest that a positive feedback loop exists between TXNDC5 and HIF signaling during hypoxia.

To further investigate whether HIF signaling is required for the pathogenic effects of endothelial TXNDC5 *in vivo*, we performed a pharmacological rescue experiment using selective inhibitors of HIF-1α (PX-478) or HIF-2α (PT-2385). Mice were administered AAV-TXN to overexpress endothelial TXNDC5 and subsequently subjected to normoxia or SuHx conditions, with or without HIF inhibitor treatment

446 (**Figure S8I**). As expected, AAV-TXN markedly exacerbated PH phenotypes, including
447 distal PA remodeling, increased RVSP, RV hypertrophy, and impaired RV function
448 under SuHx conditions. Importantly, treatment with HIF-1α or HIF-2α inhibitors
449 significantly mitigates these TXNDC5-induced vascular and cardiac abnormalities, as
450 evidenced by histological staining (**Figure 7C-F**), hemodynamic measurements
451 (**Figure S8J**), assessment of RV hypertrophy (**Figure S8K**), and echocardiographic
452 analysis (**Figure S8L-O**). Collectively, these results indicate that TXNDC5 drives PH
453 progression in a HIF signaling-dependent manner, establishing a functional TXNDC-
454 HIF positive feedback loop.
455
456 **TXNDC5 Requires BGN to Inhibit the Ubiquitination of HIF-1α/2α**
457 Interestingly, we found in the present study that the HIF-1α/2α protein levels were
458 significantly decreased by the silencing of BGN upon hypoxia exposure in hPAECs
459 (**Figure S9A**). Since TXNDC5 directly interacted with BGN, we hypothesized that the
460 regulation of HIF-1α/2α by TXNDC5 required the presence of BGN. Western blots
461 revealed that LV-TXNDC5 increased the expression of HIF-1α/2α both under normoxic
462 and hypoxic conditions in hPAECs (**Figure S9B**). More importantly, knockdown of
463 BGN abolished the upregulation of HIF-1α/2α induced by LV-TXNDC5 (**Figure 7G**).
464 These data suggest that TXNDC5 requires BGN to regulate the HIF signaling pathway.
465 Under normoxia, HIF-α is rapidly ubiquitinated by E3 ligase von Hippel-Lindau
466 (VHL) and leads to proteasomal degradation[24]. Interestingly, we found that TXNDC5
467 overexpression increased the HIF-1α/2α levels even under normoxic conditions, and
468 similar results were also observed in primary lung ECs isolated from AAV-TXN-treated
469 mice (**Figure S9C**). The protein half-life of HIF-1α/2α examined using CHX chase
470 assays showed that LV-TXNDC5-treated hPAECs displayed a prolonged half-life of
471 HIF-1α/2α as compared with control (**Figure 7H** and **Figure S9D**). We then further
472 determined whether HIF-1α/2α accumulation by TXNDC5 is VHL-dependent. It was
473 found that TXNDC5 silencing increased VHL expression, and simultaneous
474 knockdown of VHL and TXNDC5 significantly reversed the decreased HIF-1α/2α
475 protein levels caused by TXNDC5 silencing in hPAECs under hypoxic conditions

476 (**Figure 7I**). These data suggest that TXNDC5 modulates HIF-1α/2α to interfere with
477 VHL-mediated HIF-1α/2α degradation. To investigate whether TXNDC5 inhibits HIF-
478 1α/2α stability dependent on BGN, we performed *in vivo* ubiquitination assays. Results
479 showed that LV-TXNDC5 significantly suppressed the ubiquitination of HIF-1α/2α,
480 while siBGN increased it by upregulating the expression of VHL. More importantly,
481 the silencing of BGN eliminated the decrease in HIF-1α/2α ubiquitination and the
482 increase in VHL expression caused by TXNDC5 overexpression (**Figure 7J** and **Figure**
483 **S9E**). Taken together, our findings suggest that BGN is required for TXNDC5 to inhibit
484 the ubiquitination of HIF-1α/2α in a VHL-dependent manner.
485
486 **E64FC26 Exhibits Therapeutic Effects Against PH in Rats**
487 E64FC26 is a potent PDI pan-inhibitor, with IC_{50} of 16.3 μM against TXNDC5[25].
488 To evaluate the toxicity and safety of E64FC26, we performed histological analyses on
489 the major organs of rats continuously treated with E64FC26 for 5 weeks under
490 normoxic conditions. In the kidneys, the renal tubules and glomeruli maintained their
491 integrity, with no signs of tubular dilation, epithelial cell injury, necrosis, or noticeable
492 inflammatory cell infiltration in the kidneys. Similarly, hepatocytes were well-
493 organized with clear cell boundaries, and there were no indications of necrosis, cell
494 swelling, or inflammatory cell infiltration in the liver. Histological examination of the
495 spleen revealed intact white and red pulp structures, without evidence of lymphoid
496 depletion, congestion, or inflammatory infiltration (**Figure S10A**). Furthermore, body
497 weight measurements showed no significant differences in both male and female rats
498 after E64FC26 treatment compared with the vehicle (**Figure S10B**). These findings
499 collectively indicate that E64FC26 exhibits a favorable safety profile without causing
500 overt organ or systemic toxicity.
501 Then, to examine whether pharmacological inhibition of TXNDC5 activity
502 produces a therapeutic effect on PH, E64FC26 was administered intraperitoneally in
503 SuHx-induced PH rats (**Figure 8A**). Hemodynamic measurements and morphometric
504 analysis demonstrated that E64FC26 administration attenuated the elevation of RVSP
505 (**Figure 8B**) and the increase in RV/(LV+S) ratio (**Figure 8C**) in SuHx-induced PH rats

compared with those with vehicle treatment. Histological analyses revealed that E64FC26 reversed SuHx-induced PA remodeling compared with vehicle-treated rats, as evidenced by reduced distal PA muscularization, decreased medial wall thickness, and attenuated collagen deposition area (**Figure 8D** and **Figure S10C-E**). Echocardiographic assessment further indicated that E64FC26 alleviated RV dysfunction in SuHx-induced PH rats, as reflected by increased PAT/PET and TAPSE, improved RVFAC, and reduced RVFWT (**Figure S10F**). Consistent with the echocardiographic improvements, histological analyses revealed that E64FC26 administration significantly reversed the RV hypertrophy (**Figure 8E**) and reduced the RV fibrosis area (**Figure 8F**) in SuHx-induced PH rats compared with those treated with vehicle.

To assess whether the therapeutic effects of E64FC26 in PH *in vivo* are primarily mediated through TXNDC5 rather than off-target inhibition of other PDI family members, we treated TXNDC5^{ECKO} mice with E64FC26 under SuHx conditions (**Figure 8G**). Notably, E64FC26 treatment also exhibited therapeutic effects in TXNDC5$^{f/f}$ mice against SuHx challenged, consistent with the results observed in rats. More importantly, in TXNDC5 endothelial-deficient mice, administration of E64FC26 did not confer additional protection against SuHx-induced distal PA remodeling, as indicated by unchanged medial wall thickness and collagen deposition area compared with vehicle-treated TXNDC5^{ECKO} mice (**Figure 8H** and **Figure S10G-H**). Similarly, lung angiography showed that E64FC26 administration failed to improve distal pulmonary perfusion in SuHx-treated TXNDC5^{ECKO} mice (**Figure 8I**). Consistently, E64FC26 also did not attenuate RVSP elevation (**Figure S10I**), RV hypertrophy (**Figure S10J**), and RV functional impairment (**Figure S10K**) in these mice. These findings indicated that the therapeutic effect of E64FC26 in PH would be largely dependent on the targeting of endothelial TXNDC5 rather than off-target inhibition of other PDI family members. In a word, these results indicate that pharmacological inhibition of TXNDC5 activity may be a promising strategy to alleviate the progression of PH.

536 **Pulmonary Endothelium-Targeted TXNDC5 Gene Therapy Ameliorates PH**

537 We further established a pulmonary endothelium-targeted gene therapy approach
538 to enhance organ specificity. Using a self-complementary adeno-associated virus
539 (scAAV) vector encoding shRNA against TXNDC5 (shTXN), we achieve rapid and
540 endothelial-specific gene silencing *in vivo*. The vector was administered via the tail vein
541 to SuHx-induced PH rats to selectively suppress TXNDC5 in lung ECs and evaluate its
542 therapeutic efficacy (**Figure 8J**). *Ex vivo* imaging confirmed efficient lung targeting of
543 the AAV (**Figure 8K**), and Western blotting demonstrated marked suppression of
544 TXNDC5 expression in primary rat lung ECs (**Figure S10L**).

545 Treatment with shTXN significantly attenuated SuHx-induced PA remodeling
546 compared with rats receiving the control vector (shNC), as evidenced by reduced distal
547 PA muscularization, decreased medial wall thickness, and lower collagen deposition
548 area (**Figure 8L** and **Figure S10M-O**). Hemodynamic measurements further
549 demonstrated that shTXN administration attenuated the elevation of RVSP in SuHx-
550 induced PH rats (**Figure 8M**). Moreover, morphological and histological analyses
551 showed that shTXN decreased the RV/(LV+S) ratio (**Figure S10P**) and alleviated RV
552 wall thickening (**Figure 8N**). Consistently, echocardiographic assessment revealed
553 improved RV function, reflected by increased PAT/PET, TAPSE, RVFAC, and reduced
554 RVFWT (**Figure S10Q**). These findings demonstrate that endothelial-targeted
555 TXNDC5 silencing effectively mitigates pulmonary vascular remodeling and right
556 heart dysfunction in PH. Collectively, these findings demonstrate that endothelial-
557 targeted TXNDC5 silencing effectively mitigates pulmonary vascular remodeling and
558 right heart dysfunction in PH, highlighting the therapeutic potential of TXNDC5
559 inhibition.

560

561 # DISCUSSION

562 PDI family catalyzes the formation and rearrangement of disulfide bonds of
563 proteins in the endoplasmic reticulum. They play crucial roles in protein folding and
564 disulfide bond formation. In the present study, we utilized 4D label-free proteomics to

565 profile the PDI proteins in the lungs of patients with hypoxic PH, identifying TXNDC5
566 as the most significantly altered member in the PDI family. TXNDC5, dominantly
567 expressed in endothelial cells, is also known as endothelial PDI (Endo-PDI)[26]. We
568 found that the silencing of TXNDC5 inhibited the proliferation and migration of
569 hPAECs, whereas its overexpression led to changes in the cytoskeletal architecture of
570 hPAECs, implying a critical role of TXNDC5 in endothelial dysfunction in PH. In *in*
571 *vivo* studies, we found that global or endothelial-specific TXNDC5 deficiency
572 attenuated, whereas pulmonary endothelial-specific TXNDC5 overexpression
573 aggravated SuHx-induced PH. E64FC26, a pan-PDI inhibitor with IC50 of 16.3 μM
574 against TXNDC5, effectively delayed the progression of multiple myeloma *in vivo* in
575 the previous study[25]. We demonstrated in the present study that E64FC26
576 administration successfully alleviated the PA remodeling and RV hypertrophy,
577 effectively preventing the development and progression of SuHx-induced PH in rats.
578 Notably, administration of E64FC26 did not confer additional protection in endothelial
579 TXNDC5-deficient mice, indicating that its therapeutic effects are largely dependent
580 on endothelial TXNDC5. Collectively, these findings indicate that targeting TXNDC5
581 could be a promising strategy to treat PH.

582 We next examined the molecular mechanisms of the critical role of TXNDC5 in
583 PH development. Recent studies have demonstrated that alterations in ECM
584 composition and stiffness contribute to the pathological changes observed in PH,
585 influencing vascular resistance and exacerbating disease progression[27]. More
586 importantly, ECM remodeling is the cause rather than a consequence of pulmonary
587 vascular remodeling in PH[19]. We identified in the present study that TXNDC5 might
588 play a central role in orchestrating ECM homeostasis in hypoxic PH. Specifically,
589 TXNDC5 modulated proteoglycans and glycoproteins, which determine ECM stiffness
590 and elasticity, as well as collagens that define ECM structural integrity. Additionally,
591 TXNDC5 regulated matrix modulators and adhesion proteins involved in ECM
592 crosslinking, along with metallopeptidases responsible for ECM degradation and
593 turnover. Furthermore, TXNDC5 influenced basement membrane proteins,
594 angiogenesis, and growth factor-associated proteins, contributing to endothelial barrier

595 function and vascular homeostasis. More importantly, we demonstrated that POSTN,
596 BGN, LOX, and TGM2 were excessively deposited in the PAs of TXNDC5$^{f/f}$ mice but
597 were significantly reduced in TXNDC5^{ECKO} mice under SuHx conditions. As key
598 proteoglycans, POSTN and BGN regulate ECM organization and mechanotransduction,
599 contributing to vascular stiffening[28–30]. Meanwhile, LOX and TGM2, categorized under
600 matrix modulators, facilitate ECM crosslinking and collagen stabilization, further
601 exacerbating pulmonary vascular remodeling[31,32]. These findings imply that TXNDC5
602 inhibition shifts the ECM equilibrium toward a less fibrotic and more compliant
603 phenotype, mitigating PH progression by preserving vascular ECM homeostasis.

604 BGN has been demonstrated to play a significant role in clinical conditions related
605 to inflammation, metabolic disturbances, musculoskeletal irregularities, and
606 tumorigenesis[33]. We found in the present study that BGN was a direct binding partner
607 of TXNDC5, with enhanced interaction with hypoxia stimulation. Mutations at Cys89
608 and Gly351 of TXNDC5 significantly disrupted the association between TXNDC5 and
609 BGN. Notably, both amino acids were within the PDI active domain of TXNDC5,
610 implying that its PDI activity is directly involved in mediating BGN binding and
611 stabilization. Additionally, WT-TXNDC5, but not PDI-inactive TXNDC5 mutant,
612 markedly increased the FRET efficiency in the BGN folding assay. These findings
613 suggest that TXNDC5 facilitates BGN folding dependent on PDI activity, which is
614 essential for the maturation and secretion of BGN as well as many other ECM proteins.
615 Further investigation revealed that BGN was upregulated in the lungs of PH patients
616 and rodent models, particularly in the intima of remodeled pulmonary arteries.
617 Endothelial cell-specific deficiency of BGN alleviated PH progression in mice,
618 implying that targeting endothelial-derived BGN may be a potential therapeutic
619 strategy for PH. Importantly, endothelial-specific deficiency of BGN restored distal PA
620 remodeling and RV hypertrophy induced by TXNDC5 overexpression in mice,
621 indicating that BGN is a critical downstream effector mediating TXNDC5-driven PH.
622 Additionally, rhBGN promoted the proliferation and apoptosis resistance of hPASMCs,
623 suggesting that extracellular BGN also contributes to vascular remodeling. More
624 importantly, we found that serum BGN level was significantly increased in PH patients

625 and was perfectly correlated with the disease severity. Our data, therefore, highlighted
626 a potential for BGN to be a diagnostic biomarker of PH.

627 HIF signaling is one of the most dominant pathways involved in the development
628 of hypoxic PH[34]. HIF-α subunits are rapidly degraded under normoxic conditions by
629 the VHL E3 ligase[35]. In the present study, we demonstrated that silencing of BGN
630 effectively abolished the upregulation of HIF-1α/2α induced by TXNDC5
631 overexpression and restored HIF-1α/2α ubiquitination by relieving VHL inhibition.
632 These findings provide new insights into how ECM remodeling is coordinated with
633 hypoxia-driven cellular responses in PH. Given that TXNDC5 potentially regulates
634 ECM homeostasis and the established interplay between ECM and the HIF pathway,
635 we speculate that factors form a complex regulatory network that contributes to the PH
636 progression. Whether other ECM components are involved in the TXNDC5-HIF axis
637 warrants further investigation. Taken together, targeting TXNDC5 may offer
638 therapeutic strategies for regulating both ECM dynamics and hypoxic signaling.

639 Evidence has shown that excessive depletion of HIF-1α or HIF-2α may lead to
640 organ dysfunction, developmental defects, and even embryonic lethality in mice[36–38].
641 This highlights the potential risks of systemic HIF inhibition. Interestingly, although
642 clinical trial data are not yet available, preclinical studies have shown that various
643 small-molecule HIF inhibitors exhibit promising therapeutic effects in PH models[34]. In
644 the present study, we demonstrated that TXNDC5 is primarily expressed and
645 upregulated in endothelial cells. Targeting TXNDC5 may offer a more tissue-specific
646 approach to inhibit HIF signaling, thereby potentially reducing or avoiding the systemic
647 side effects. Notably, global TXNDC5 knockout prevented SuHx-induced HIF
648 signaling activation, without causing any adverse effects on growth and organ
649 development in mice. These findings suggest that targeting TXNDC5 blocks HIF-
650 driven pathological processes in PH, offering a promising alternative to HIF inhibition
651 with better tissue specificity and fewer adverse effects.

652 In summary, we identified for the first time the novel role of PDI protein TXNDC5
653 in the pathogenesis of hypoxic PH. TXNDC5 facilitates ECM protein (e.g., BGN)
654 folding and reduces HIF-1α/2α ubiquitination, which contributes to endothelial

dysfunction. TXNDC5 promotes a positive feedback loop between BGN and HIF signaling, driving the progression of pulmonary vascular remodeling in PH. This study highlights TXNDC5 as a promising therapeutic target for hypoxia-induced PH and lays the groundwork for future clinical investigations.

Acknowledgments

We thank Professor John Shyy from the University of California, San Diego, United States, for critical reading and advice on this article.

Sources of Funding

This work was supported by the Key Program of National Natural Science Foundation of China (NSFC, grant No. 82430004 to Jin-Song Bian), Shenzhen Science Fund for Distinguished Young Scholars (grant No. RCJC20210706091946002 to Xiaowei Nie), Shenzhen Science and Technology Program (grant No. GJHZ20240218111401002 to Jin-Song Bian), and the National Natural Science Foundation of China (NSFC, grant No. 82241021 to Xiaowei Nie).

References

1. Johnson S, Sommer N, Cox-Flaherty K, Weissmann N, Ventetuolo CE, Maron BA. Pulmonary Hypertension: A Contemporary Review. *Am J Respir Crit Care Med*. 2023;208:528–548. doi: 10.1164/rccm.202302-0327SO

2. Shlobin OA, Adir Y, Barbera JA, Cottin V, Harari S, Jutant E-M, Pepke-Zaba J, Ghofrani H-A, Channick R. Pulmonary hypertension associated with lung diseases. *Eur Respir J*. 2024;64:2401200. doi: 10.1183/13993003.01200-2024

3. Evans CE, Cober ND, Dai Z, Stewart DJ, Zhao Y-Y. Endothelial cells in the pathogenesis of pulmonary arterial hypertension. *Eur Respir J*. 2021;58:2003957. doi: 10.1183/13993003.03957-2020

4. Ma B, Cao Y, Qin J, Chen Z, Hu G, Li Q. Pulmonary artery smooth muscle cell phenotypic switching: A key event in the early stage of pulmonary artery hypertension. *Drug Discov Today*. 2023;28:103559. doi: 10.1016/j.drudis.2023.103559

686 5. Mandras SA, Mehta HS, Vaidya A. Pulmonary Hypertension: A Brief Guide for
687 Clinicians. *Mayo Clin Proc*. 2020;95:1978–1988. doi:
688 10.1016/j.mayocp.2020.04.039

689 6. Olsson KM, Corte TJ, Kamp JC, Montani D, Nathan SD, Neubert L, Price LC,
690 Kiely DG. Pulmonary hypertension associated with lung disease: new insights
691 into pathomechanisms, diagnosis, and management. *Lancet Respir Med*.
692 2023;11:820–835. doi: 10.1016/S2213-2600(23)00259-X

693 7. Kanemura S, Matsusaki M, Inaba K, Okumura M. PDI Family Members as Guides
694 for Client Folding and Assembly. *Int J Mol Sci*. 2020;21:9351. doi:
695 10.3390/ijms21249351

696 8. Kuramochi T, Yamashita Y, Arai K, Kanemura S, Muraoka T, Okumura M.
697 Boosting the enzymatic activity of CxxC motif-containing PDI family members.
698 *Chem Commun (Camb)*. 2024;60:6134–6137. doi: 10.1039/d4cc01712a

699 9. Rahman NSA, Zahari S, Syafruddin SE, Firdaus-Raih M, Low TY, Mohtar MA.
700 Functions and mechanisms of protein disulfide isomerase family in cancer
701 emergence. *Cell Biosci*. 2022;12:129. doi: 10.1186/s13578-022-00868-6

702 10. Kobayashi Y, Oguro A, Hirata Y, Imaoka S. The regulation of Hypoxia-Inducible
703 Factor-1 (HIF-1alpha) expression by Protein Disulfide Isomerase (PDI). *PLoS*
704 *One*. 2021;16:e0246531. doi: 10.1371/journal.pone.0246531

705 11. Nagarkoti S, Kim Y-M, Ash D, Das A, Vitriol E, Read T-A, Youn S-W, Sudhahar
706 V, McMenamin M, Hou Y, et al. Protein disulfide isomerase A1 as a novel redox
707 sensor in VEGFR2 signaling and angiogenesis. *Angiogenesis*. 2023;26:77–96. doi:
708 10.1007/s10456-022-09852-7

709 12. Hung C-T, Tsai Y-W, Wu Y-S, Yeh C-F, Yang K-C. The novel role of ER protein
710 TXNDC5 in the pathogenesis of organ fibrosis: mechanistic insights and
711 therapeutic implications. *J Biomed Sci*. 2022;29:63. doi: 10.1186/s12929-022-
712 00850-x

713 13. Jin Y, Sharma A, Bai S, Davis C, Liu H, Hopkins D, Barriga K, Rewers M, She J-
714 X. Risk of type 1 diabetes progression in islet autoantibody-positive children can
715 be further stratified using expression patterns of multiple genes implicated in
716 peripheral blood lymphocyte activation and function. *Diabetes*. 2014;63:2506–
717 2515. doi: 10.2337/db13-1716

718 14. Wang L, Dong H, Song G, Zhang R, Pan J, Han J. TXNDC5 synergizes with
719 HSC70 to exacerbate the inflammatory phenotype of synovial fibroblasts in
720 rheumatoid arthritis through NF-κB signaling. *Cell Mol Immunol*. 2018;15:685–
721 696. doi: 10.1038/cmi.2017.20

722 15. Wang X, Li H, Chang X. The role and mechanism of TXNDC5 in diseases. *Eur J*

723 *Med Res*. 2022;27:145. doi: 10.1186/s40001-022-00770-4

724 16. Yeh C-F, Cheng S-H, Lin Y-S, Shentu T-P, Huang R-T, Zhu J, Chen Y-T, Kumar
725 S, Lin M-S, Kao H-L, et al. Targeting mechanosensitive endothelial TXNDC5 to
726 stabilize eNOS and reduce atherosclerosis in vivo. *Sci Adv*. 2022;8:eabl8096. doi:
727 10.1126/sciadv.abl8096

728 17. Wu S, Luo X, Chen Y, Wang Z, Liu X, Sun N, Zhao J, Luo W, Zhang J, Tong X,
729 et al. Sodium-glucose cotransporter 2 inhibitors attenuate vascular calcification by
730 suppressing endoplasmic reticulum protein thioredoxin domain containing 5
731 dependent osteogenic reprogramming. *Redox Biol*. 2024;73:103183. doi:
732 10.1016/j.redox.2024.103183

733 18. Fu Y, Zhou Y, Wang K, Li Z, Kong W. Extracellular Matrix Interactome in
734 Modulating Vascular Homeostasis and Remodeling. *Circ Res*. 2024;134:931–949.
735 doi: 10.1161/CIRCRESAHA.123.324055

736 19. Thenappan T, Chan SY, Weir EK. Role of extracellular matrix in the pathogenesis
737 of pulmonary arterial hypertension. *Am J Physiol Heart Circ Physiol*.
738 2018;315:H1322–H1331. doi: 10.1152/ajpheart.00136.2018

739 20. Nie X, Shen C, Tan J, Wu Z, Wang W, Chen Y, Dai Y, Yang X, Ye S, Chen J, et al.
740 Periostin: A Potential Therapeutic Target For Pulmonary Hypertension? *Circ Res*.
741 2020;127:1138–1152. doi: 10.1161/CIRCRESAHA.120.316943

742 21. Bian J-S, Chen J, Zhang J, Tan J, Chen Y, Yang X, Li Y, Deng L, Chen R, Nie X.
743 ErbB3 Governs Endothelial Dysfunction in Hypoxia-Induced Pulmonary
744 Hypertension. *Circulation*. 2024;150:1533–1553. doi:
745 10.1161/CIRCULATIONAHA.123.067005

746 22. Zhang Y, Li X, Li S, Zhou Y, Zhang T, Sun L. Immunotherapy for Pulmonary
747 Arterial Hypertension: From the Pathogenesis to Clinical Management. *Int J Mol*
748 *Sci*. 2024;25:8427. doi: 10.3390/ijms25158427

749 23. Shih Y-C, Chen C-L, Zhang Y, Mellor RL, Kanter EM, Fang Y, Wang H-C, Hung
750 C-T, Nong J-Y, Chen H-J, et al. Endoplasmic Reticulum Protein TXNDC5
751 Augments Myocardial Fibrosis by Facilitating Extracellular Matrix Protein
752 Folding and Redox-Sensitive Cardiac Fibroblast Activation. *Circ Res*.
753 2018;122:1052–1068. doi: 10.1161/CIRCRESAHA.117.312130

754 24. Luo Z, Tian M, Yang G, Tan Q, Chen Y, Li G, Zhang Q, Li Y, Wan P, Wu J.
755 Hypoxia signaling in human health and diseases: implications and prospects for
756 therapeutics. *Signal Transduct Target Ther*. 2022;7:218. doi: 10.1038/s41392-
757 022-01080-1

758 25. Robinson RM, Reyes L, Duncan RM, Bian H, Reitz AB, Manevich Y, McClure
759 JJ, Champion MM, Chou CJ, Sharik ME, et al. Inhibitors of the protein disulfide

isomerase family for the treatment of multiple myeloma. *Leukemia*. 2019;33:1011–1022. doi: 10.1038/s41375-018-0263-1

26. Sullivan DC, Huminiecki L, Moore JW, Boyle JJ, Poulsom R, Creamer D, Barker J, Bicknell R. EndoPDI, a novel protein-disulfide isomerase-like protein that is preferentially expressed in endothelial cells acts as a stress survival factor. *J Biol Chem*. 2003;278:47079–47088. doi: 10.1074/jbc.M308124200

27. Jandl K, Radic N, Zeder K, Kovacs G, Kwapiszewska G. Pulmonary vascular fibrosis in pulmonary hypertension - The role of the extracellular matrix as a therapeutic target. *Pharmacol Ther*. 2023;247:108438. doi: 10.1016/j.pharmthera.2023.108438

28. Sun X-J, Ma W-Q, Zhu Y, Liu N-F. POSTN promotes diabetic vascular calcification by interfering with autophagic flux. *Cell Signal*. 2021;83:109983. doi: 10.1016/j.cellsig.2021.109983

29. Nikoloudaki G, Snider P, Simmons O, Conway SJ, Hamilton DW. Periostin and matrix stiffness combine to regulate myofibroblast differentiation and fibronectin synthesis during palatal healing. *Matrix Biol*. 2020;94:31–56. doi: 10.1016/j.matbio.2020.07.002

30. Yu M, He X, Song X, Gao J, Pan J, Zhou T, Wang Q, Zhu W, Ma H, Zeng H, et al. Biglycan promotes hepatic fibrosis through activating heat shock protein 47. *Liver Int*. 2023;43:500–512. doi: 10.1111/liv.15477

31. Wang Z-J, Guan Q-W, Zhou H-H, Mao X-Y, Chen F-H. Mechanistic insight into lysyl oxidase in vascular remodeling and angiogenesis. *Genes Dis*. 2023;10:771–785. doi: 10.1016/j.gendis.2022.05.011

32. Zhang M, Li L, Zhang W, Li M, Yan G, Tang C. TG2 participates in pulmonary vascular remodelling by regulating the senescence of pulmonary artery smooth muscle cells. *Cell Signal*. 2024;121:111296. doi: 10.1016/j.cellsig.2024.111296

33. Appunni S, Rubens M, Ramamoorthy V, Anand V, Khandelwal M, Sharma A. Biglycan: an emerging small leucine-rich proteoglycan (SLRP) marker and its clinicopathological significance. *Mol Cell Biochem*. 2021;476:3935–3950. doi: 10.1007/s11010-021-04216-z

34. Pullamsetti SS, Mamazhakypov A, Weissmann N, Seeger W, Savai R. Hypoxia-inducible factor signaling in pulmonary hypertension. *J Clin Invest*. 2020;130:5638–5651. doi: 10.1172/JCI137558

35. Tarade D, Ohh M. The HIF and other quandaries in VHL disease. *Oncogene*. 2018;37:139–147. doi: 10.1038/onc.2017.338

36. Kotch LE, Iyer NV, Laughner E, Semenza GL. Defective vascularization of HIF-

1alpha-null embryos is not associated with VEGF deficiency but with mesenchymal cell death. *Dev Biol*. 1999;209:254–267. doi: 10.1006/dbio.1999.9253

37. Chen H, Houshmand G, Mishra S, Fong G-H, Gittes GK, Esni F. Impaired pancreatic development in Hif2-alpha deficient mice. *Biochem Biophys Res Commun*. 2010;399:440–445. doi: 10.1016/j.bbrc.2010.07.111

38. Peng Y-J, Nanduri J, Khan SA, Yuan G, Wang N, Kinsman B, Vaddi DR, Kumar GK, Garcia JA, Semenza GL, et al. Hypoxia-inducible factor 2α (HIF-2α) heterozygous-null mice exhibit exaggerated carotid body sensitivity to hypoxia, breathing instability, and hypertension. *Proc Natl Acad Sci U S A*. 2011;108:3065–3070. doi: 10.1073/pnas.1100064108

Figure legends

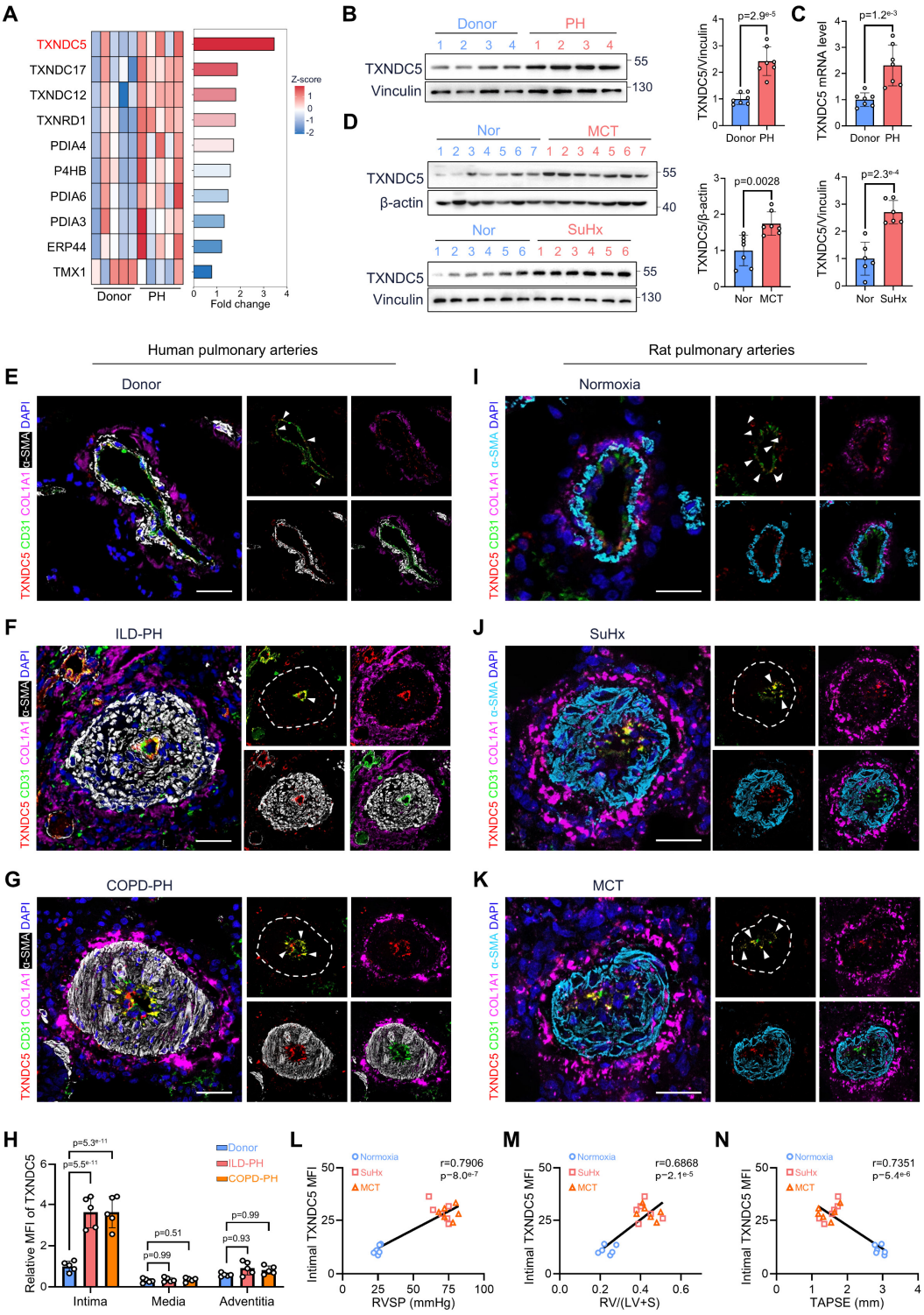

Figure 1. TXNDC5 was upregulated in PH.

A, Heatmap of 4D label-free proteomics showing PDI family expression in lung tissues from 5 non-PH donors and 5 patients with hypoxic PH. **B**, Representative Western blots and quantification of TXNDC5 and Vinculin in the lungs of control donors and PH

815 patients (n=7). **C**, qPCR analysis of TXNDC5 mRNA levels in lung homogenates from
816 donors and patients with PH (n=7). **D**, Western blots showing the TXNDC5 protein
817 levels in the lungs collected from MCT (n=7) or SuHx-treated rats (n=6) or rats under
818 normoxia. **E**, **F**, and **G**, Representative confocal images of multiplex
819 immunofluorescence (mIF) staining for TXNDC5 (red), CD31 (green), α-SMA (white),
820 and COL1A1 (purple) in distal pulmonary arteries (PAs) from donors, ILD-PH, and
821 COPD-PH patients. Nuclei were counterstained with DAPI (blue). White arrows
822 indicate the colocalization of TXNDC5 with CD31 (yellow). White dashed lines
823 indicate the outer layer of smooth muscle cells. Scale bars=25 μm. **H**, Quantitative
824 analysis showing elevated TXNDC5 mean fluorescence intensity (MFI) in the $CD31^+$
825 intima of distal PAs from patients with ILD-PH and COPD-PH compared with non-PH
826 donors. (n=5). **I**, **J**, and **K**, Representative images of mIF staining for TXNDC5 (red),
827 CD31 (green), α-SMA (cyan), and COL1A1 (purple) in distal PAs from SuHx- or
828 MCT-treated rats or rats under normoxia. Nuclei were counterstained with DAPI (blue).
829 White arrows indicate the colocalization of TXNDC5 with CD31 (yellow). White
830 dashed lines indicate the outer layer of smooth muscle cells. Scale bars=20 μm. **L**, **M**,
831 and **N**, Correlation analyses of intimal TXNDC5 MFI and right ventricular systolic
832 pressure (RVSP), Fulton index [RV/(LV+S)], and tricuspid annular plane systolic
833 excursion (TAPSE) in rats. Data represent the mean±SD. Comparisons of parameters
834 were performed with the unpaired 2-tailed Student *t*-test (**B-D**) or 2-way ANOVA (**H**),
835 followed by Tukey honestly significant difference test for multiple comparisons and the
836 Pearson correlation test (**L-N**). PDI indicates protein disulfide isomerase; PH,
837 pulmonary hypertension; TXNDC5, thioredoxin domain containing 5; α-SMA, α-
838 smooth muscle actin; COL1A1, collagen type I alpha 1; DAPI, 4′,6-diamidino-2-
839 phenylindole; Nor, normoxia; SuHx, Sugen5416/hypoxia; and MCT, monocrotaline.

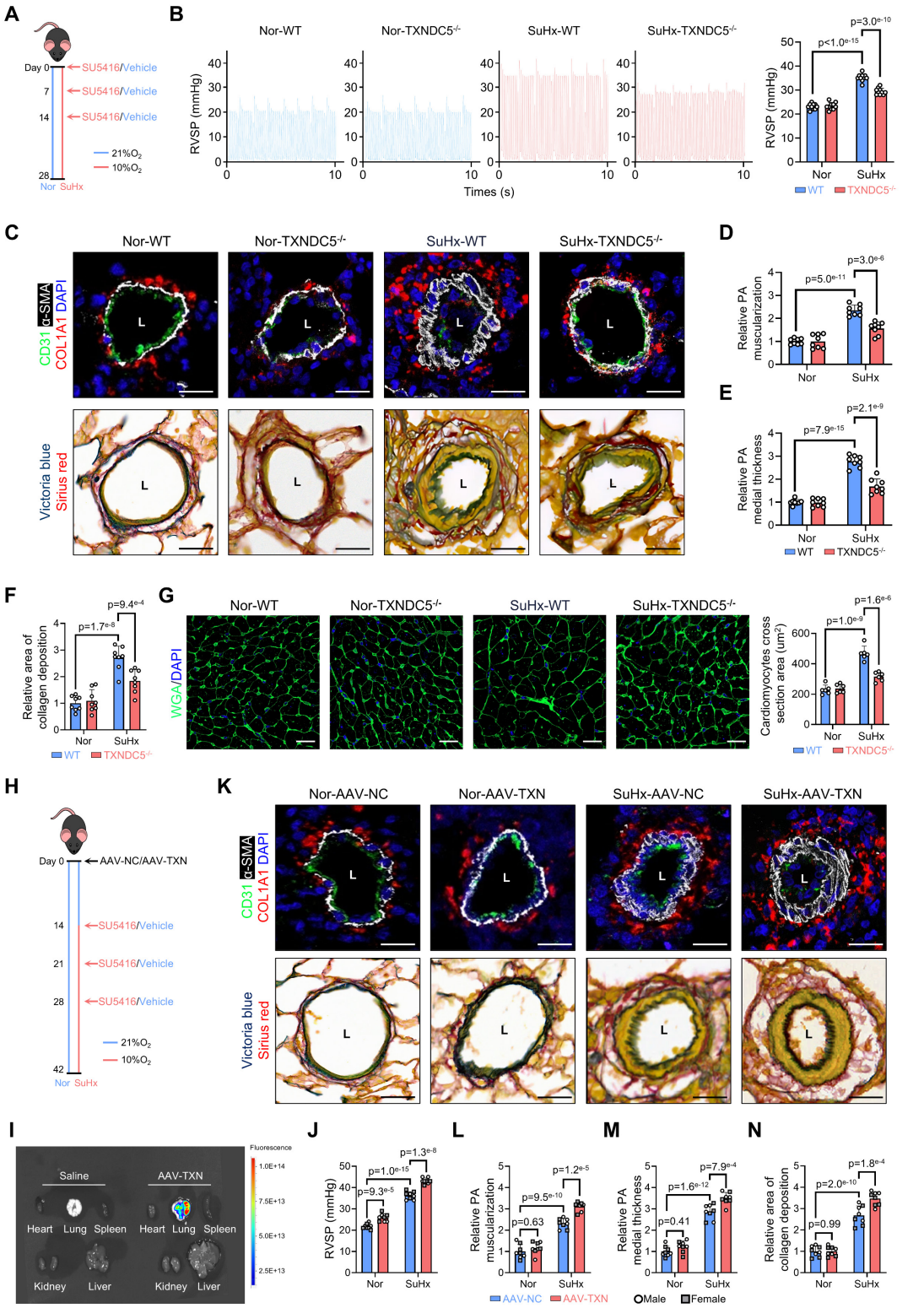

Figure 2. TXNDC5 contributed to SuHx-induced pulmonary vascular remodeling

A, Schematic protocol for the animal treatments in the SuHx-induced PH mice. **B**, Representative tracings and quantification of right ventricular systolic pressure (RVSP) in male WT and TXNDC5$^{-/-}$ mice exposed to normoxia or SuHx (n=10). **C**,

845 Representative multiplex immunofluorescence (mIF) for CD31 (green), α-SMA (white),
846 and COL1A1 (red), and Victoria blue/Sirius red (VB/SR) staining for elastic lamina
847 (dark blue), collagens (red), and muscle fiber (yellow) in distal pulmonary arteries (PAs)
848 from male WT and TXNDC5$^{-/-}$ mice exposed to normoxia or SuHx. Nuclei were
849 counterstained with DAPI (blue). L indicates lumen. Scale bars=25 μm. **D**,
850 Quantification of distal PA muscularization based on α-SMA positive area in WT and
851 TXNDC5$^{-/-}$ mice exposed to normoxia or SuHx (n=8). **E**, Measurement of medial wall
852 thickness in distal PAs, defined by the elastic lamina visualized with VB staining (n=8).
853 **F**, Quantification of collagen deposition area in distal PAs based on SR staining,
854 indicating decreased collagen deposition in TXNDC5-deficient mice (n=8). **G**,
855 Immunofluorescence staining of WGA (green) in right ventricles from male WT and
856 TXNDC5$^{-/-}$ mice exposed to normoxia or SuHx (n=6). Nuclei were counterstained with
857 DAPI (blue). Scale bars=20 μm. **H**, Schematic diagram illustrating the *in vivo*
858 pulmonary endothelial-specific overexpression of TXNDC5 in both male and female
859 mice. Mice received a single tail vein injection of AAV-NC or AAV-TXN at the
860 beginning of the 2 weeks, followed by SuHx exposure. **I**, Representative images of
861 major organs from saline-treated control or AAV-TXN-treated mice, showing GFP
862 fluorescence delivered by AAV detected by IVIS imaging system. **J**, Hemodynamic
863 measurements of RVSP in male and female mice administered with AAV-NC or AAV-
864 TXN under normoxia or SuHx situations (n=8). **K**, Representative mIF of distal PAs
865 from AAV-NC or AAV-TXN-treated male and female mice under SuHx or normoxia,
866 showing CD31 (green), α-SMA (white), and COL1A1 (red), together with VB/SR
867 staining of elastic lamina (dark blue), perivascular collagens (red), and muscle fiber
868 (yellow). Nuclei were counterstained with DAPI (blue). L indicates lumen. Scale
869 bars=25 μm. **L**, **M,** and **N**, Quantitative analysis of distal PA remodeling in AAV-NC or
870 AAV-TXN-treated mice under normoxic or SuHx conditions (n=8). PA muscularization,
871 medial wall thickness, and collagen deposition area were assessed using α-SMA, VB,
872 and SR staining, respectively. Data represent the mean±SD. Comparisons of parameters
873 were performed with 2-way ANOVA, followed by Tukey honestly significant
874 difference test for multiple comparisons. DAPI indicates 4′,6-diamidino-2-

875 phenylindole; α-SMA, α-smooth muscle actin; COL1A1, collagen type I alpha 1; WGA,
876 wheat germ agglutinin; GFP, green fluorescent protein; Nor, normoxia; SuHx, and
877 Sugen5416/hypoxia.

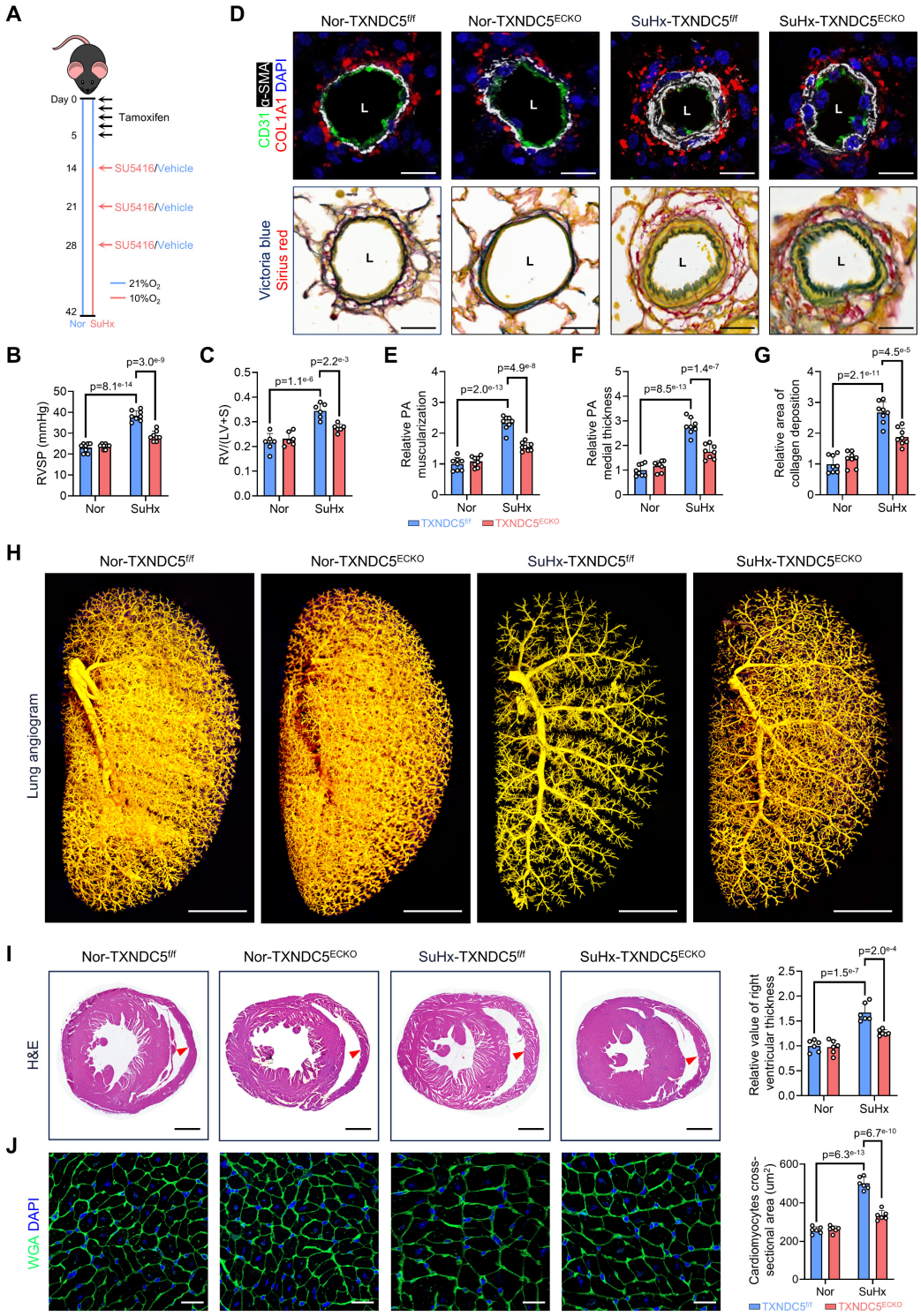

878

879 **Figure 3. Endothelial cell-specific deletion of TXNDC5 ameliorated SuHx-induced**

880 **PH.**

881 **A**, Schematic protocol for the endothelial cell-specific TXNDC5 knockout mice assays.
882 Mice were intraperitoneally injected with 75 mg/kg tamoxifen once daily for 5 days
883 before being exposed to SuHx. **B**, Hemodynamic measurements of right ventricular
884 systolic pressure (RVSP) in male TXNDC5$^{f/f}$ and TXNDC5^{ECKO} mice exposed to
885 normoxia or SuHx (n=8). **C**, Fulton index [RV/(LV+S)] in male TXNDC5$^{f/f}$ and
886 TXNDC5^{ECKO} mice (n=8). **D**, Representative multiplex immunofluorescence (mIF) of
887 distal pulmonary arteries (PAs) from male TXNDC5$^{f/f}$ and TXNDC5^{ECKO} mice under
888 normoxia or SuHx, showing CD31 (green), α-SMA (white), and COL1A1 (red),
889 together with Victoria blue/Sirius red (VB/SR) staining of elastic lamina (dark blue),
890 perivascular collagens (red), and muscle fiber (yellow). Nuclei were counterstained
891 with DAPI (blue). L indicates lumen. Scale bars=25 μm. **E**, Quantification of distal PA
892 muscularization based on α-SMA positive area (n=8). **F**, Medial wall thickness of distal
893 PAs, measured across the elastic lamina visualized by VB staining (n=8). **G**,
894 Perivascular collagen deposition quantified using SR staining (n=8). **H**, Representative
895 lung angiogram of the left lungs from TXNDC5$^{f/f}$ and TXNDC5^{ECKO} mice treated with
896 SuHx or under normoxic conditions. Scale bars=2 mm. **I**, Histological analysis of the
897 cross-sectioned heart at the mid-RV (red arrows) plane from male TXNDC5$^{f/f}$ and
898 TXNDC5^{ECKO} mice with or without SuHx exposure (n=6). Scale bars=1 mm. **J**,
899 Immunofluorescence staining of WGA (green) in RV from male TXNDC5$^{f/f}$ and
900 TXNDC5^{ECKO} mice exposed to normoxia or SuHx (n=6). Nuclei were counterstained
901 with DAPI (blue). Scale bars=20 μm. Data represent the mean±SD. Comparisons of
902 parameters were performed with 2-way ANOVA, followed by Tukey honestly
903 significant difference test for multiple comparisons. DAPI indicates 4′,6-diamidino-2-
904 phenylindole; H&E, hematoxylin-eosin; α-SMA, α-smooth muscle actin; COL1A1,
905 collagen type I alpha 1; WGA, wheat germ agglutinin; f/f, flox/flox; Nor, normoxia;
906 SuHx, Sugen5416/hypoxia; and RV, right ventricle.

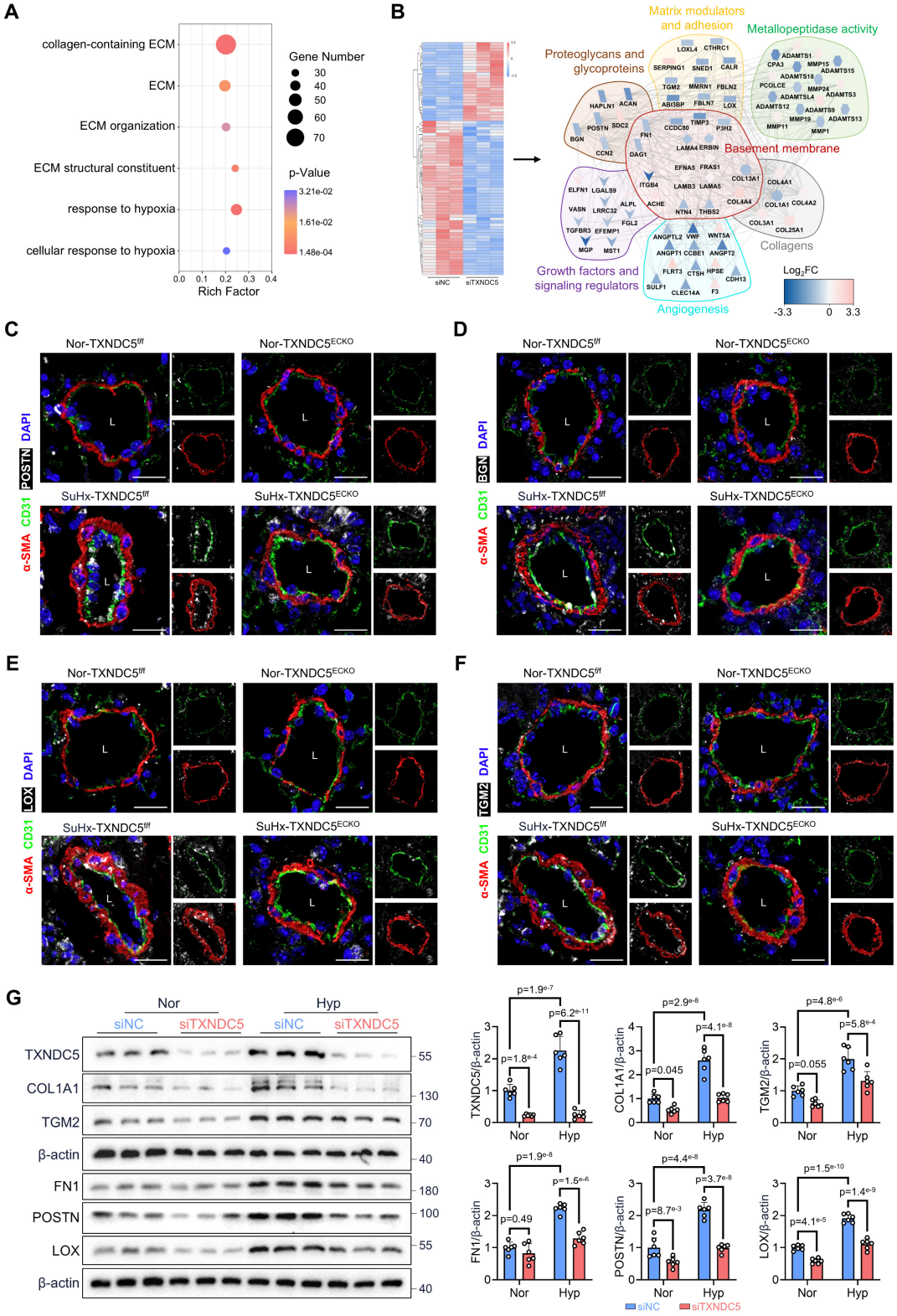

Figure 4. TXNDC5 regulated ECM protein expression and distribution.

A, HPAECs were transfected with siTXNDC5 or siNC under hypoxic conditions, followed by RNA sequencing analysis (n=3). Bubble chart showing the Gene Ontology enrichment using DAVID for the differentially expressed genes. **B**, Differentially

912 expressed ECM proteins were selected and visualized by heatmap (left). The PPI
913 network showed that TXNDC5-targeted ECM proteins could be classified into different
914 functional subgroups (right). **C**, **D**, **E**, and **F**, Representative images of
915 immunofluorescence staining of α-SMA (red), CD31 (green), and POSTN, BGN, LOX,
916 or TGM2 (white) in PAs from $TXNDC5^{f/f}$ and $TXNDC5^{ECKO}$ mice under normoxia and
917 SuHx conditions. Nuclei were counterstained with DAPI (blue). L indicates lumen.
918 Scale bars=20 μm. **G**, Western blots showing the protein levels of COL1A1, TGM2,
919 FN1, POSTN, and LOX in hPAECs transferred with siTXNDC5 or siNC in normoxia
920 or hypoxia conditions (n=6). Data represent the mean±SD. Comparisons of parameters
921 were performed with the 2-way ANOVA, followed by the Tukey honestly significant
922 difference test for multiple comparisons. ECM indicates extracellular matrix; PPI,
923 protein-protein interaction; Nor, normoxia; Hyp, hypoxia; SuHx, Sugen5416/hypoxia;
924 si, small interfering; α-SMA, α-smooth muscle actin; POSTN, periostin; BGN, biglycan;
925 LOX, lysyl oxidase; TGM2, transglutaminase 2; FN1, fibronectin; and COL1A1,
926 collagen alpha-1 chain.

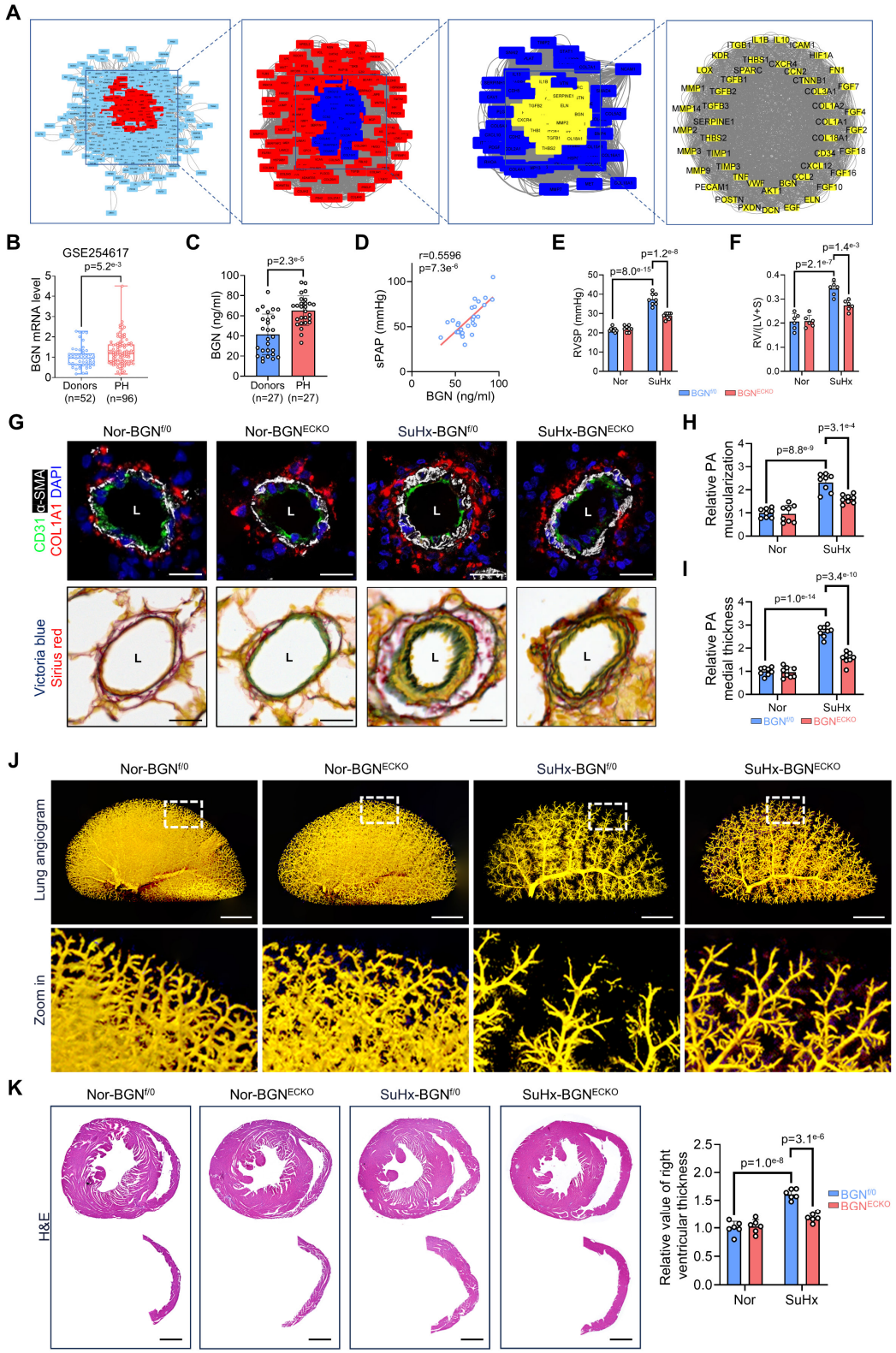

Figure 5. BGN served as a biomarker and therapeutic target of PH.

A, The progressive screening of the PPI network between ECM genes and ECs function-related genes. Each new PPI network is composed of core genes in the previous network. **B**, Box-whisker plot showing the relative mRNA levels of TXNDC5

932 in lung tissues from PH patients (n=96) and healthy donors (n=52) (GSE254617). **C**,
933 Enzyme-linked immunosorbent assay showing the BGN level in the serum of non-PH
934 donors (n=27) and patients with PH (n=27). **D**, Linear regression analysis showing the
935 correlation between serum BGN concentrations with sPAP of PH patients (n=27). **E**,
936 Quantification of right ventricular systolic pressure (RVSP) in male $BGN^{f/0}$ and
937 BGN^{ECKO} mice exposed to normoxia or SuHx (n=8). **F**, Fulton index [RV/(LV+S)] in
938 $BGN^{f/0}$ and BGN^{ECKO} mice exposed to normoxia or SuHx (n=8). **G**, Representative
939 multiplex immunofluorescence (mIF) of distal pulmonary arteries (PAs) from $BGN^{f/0}$
940 and BGN^{ECKO} mice under normoxia or SuHx, showing CD31 (green), α-SMA (white),
941 and COL1A1 (red), together with Victoria blue/Sirius red (VB/SR) staining of elastic
942 lamina (dark blue), perivascular collagens (red), and muscle fiber (yellow). Nuclei were
943 counterstained with DAPI (blue). L indicates lumen. Scale bars=25 μm. **H**,
944 Quantification of distal PA muscularization based on α-SMA positive area (n=8). **I**,
945 Medial wall thickness of distal PAs, measured across the elastic lamina visualized by
946 VB staining (n=8). **J**, Representative lung angiogram of the left lungs from $BGN^{f/0}$ and
947 BGN^{ECKO} mice treated with SuHx or under normoxic conditions. Scale bars=2 mm. **K**,
948 Histological analysis of heart cross-sections at the mid-RV plane (top) and highlighted
949 right ventricular wall (bottom) of the male $BGN^{f/0}$ and BGN^{ECKO} mice exposed to
950 normoxia or SuHx (n=6). Scale bars=1 mm. Data represent the mean±SD. Comparisons
951 of parameters were performed with the 2-tailed Mann-Whitney *U* test (**B** and **C**),
952 Pearson correlation test (**D**), or 2-way ANOVA (**E-F**, **H-I,** and **K**), followed by Tukey
953 honestly significant difference test for multiple comparisons. H&E indicates
954 hematoxylin-eosin; α-SMA, α-smooth muscle actin; COL1A1, collagen type I alpha 1;
955 DAPI, 4′,6-diamidino-2-phenylindole; f/0, flox/0; Nor, normoxia; SuHx,
956 Sugen5416/hypoxia; RV, right ventricle; and sPAP, systolic pulmonary arterial pressure.
957

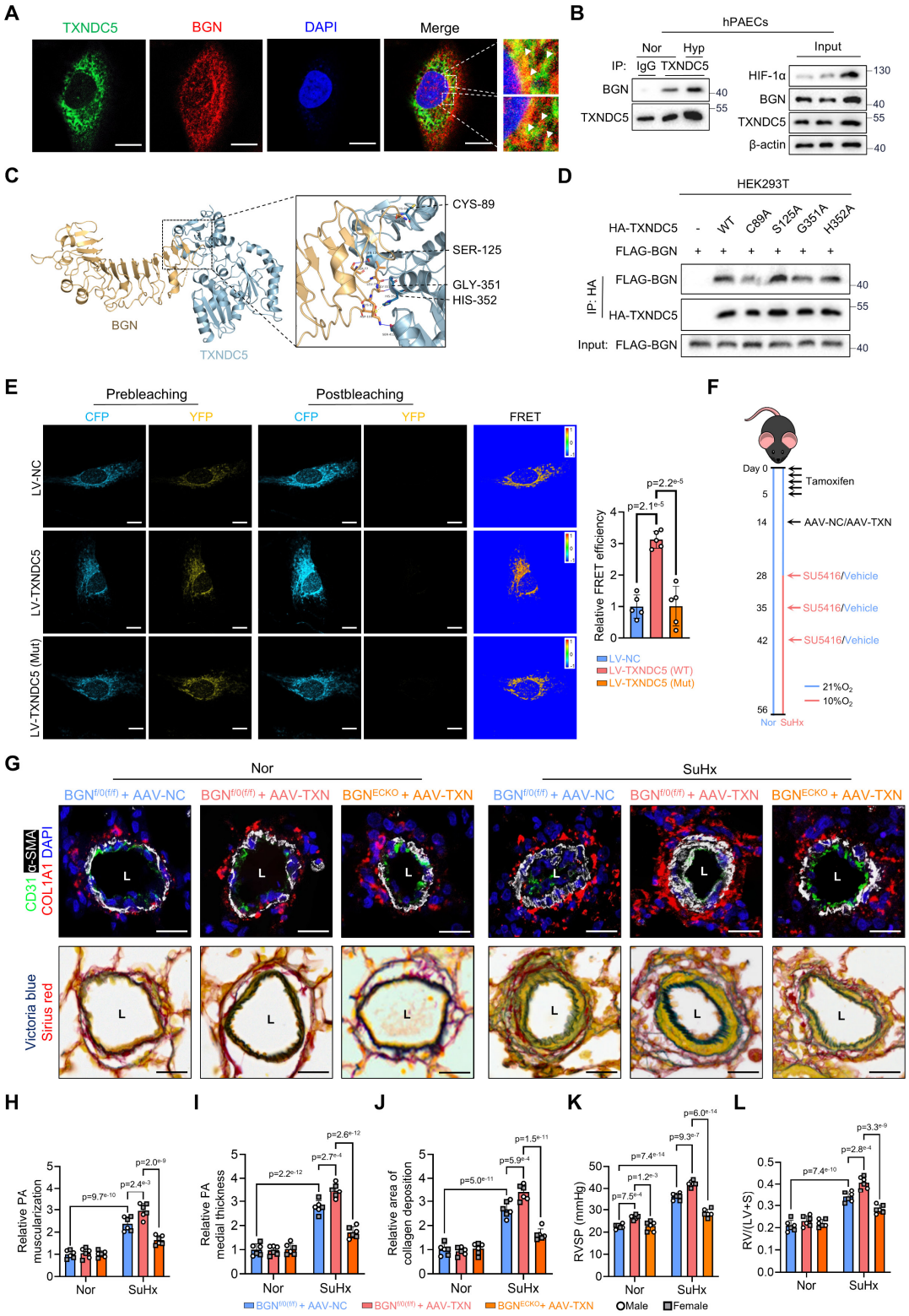

958

959 **Figure 6. TXNDC5 assisted BGN protein folding to promote PH.**

960 **A**, Immunofluorescence staining showing the localization of TXNDC5 (green) and

961 BGN (red) in hPAECs. Nuclei (blue) were stained with DAPI. White arrows in the

962 enlarged view indicate the colocalization of TXNDC5 with BGN (yellow). Scale

963 bars=10 μm. **B**, Coimmunoprecipitation analysis showing the interaction between
964 TXNDC5 and BGN in hPAECs under both normoxic and hypoxic situations. IP:
965 TXNDC5, immunoprecipitation with TXNDC5 antibody. IgG for the negative control.
966 **C**, Molecular docking showing the binding domains of human TXNDC5 and BGN. **D**,
967 Immunoprecipitation with anti-HA beads in HEK293T cells transfected with FLAG-
968 BGN and HA-TXNDC5 mutant plasmids. **E**, FRET acceptor photobleaching of the
969 hPAECs transfected with CFP-BGN-YFP plasmid. CFP and YFP images were taken
970 both before and after acceptor photobleaching. FRET efficiency is displayed as a
971 pseudocolor representation and qualification by ImageJ (n=5). Scale=10 μm. **F**,
972 Schematic of the *in vivo* rescue experiments: adeno-associated virus encoding
973 TXNDC5 (AAV-TXN) or control AAV (AAV-NC) was delivered to lung ECs in
974 $BGN^{f/0(f/f)}$ and BGN^{ECKO} mice under normoxia or SuHx conditions. **G**, Representative
975 multiplex immunofluorescence (mIF) images of distal pulmonary arteries (PAs) from
976 $BGN^{f/0(f/f)}$ and BGN^{ECKO} mice treated with AAV-NC or AAV-TXN, showing CD31
977 (green), α-SMA (white), and COL1A1 (red), with Victoria blue/Sirius red (VB/SR)
978 staining of elastic lamina (dark blue), perivascular collagens (red), and muscle fiber
979 (yellow). Nuclei stained with DAPI (blue). L indicates lumen. Scale bars=25 μm. **H**,
980 Quantification of distal PA muscularization in $BGN^{f/0(f/f)}$ and BGN^{ECKO} mice with AAV-
981 NC or AAV-TXN administration (n=6). **I**, Medial wall thickness of distal PAs measured
982 across the elastic lamina, visualized by VB staining (n=6). **J**, Quantification of collagen
983 deposition area in distal PAs (n=6). **K**, Right ventricular systolic pressure (RVSP) in
984 $BGN^{f/0(f/f)}$ and BGN^{ECKO} mice treated with AAV-NC or AAV-TXN under SuHx or
985 normoxia conditions (n=6). **L**, Fulton index [RV/(LV+S)] in $BGN^{f/0(f/f)}$ and BGN^{ECKO}
986 mice with AAV-NC or AAV-TXN treatment (n=6). Data represent the mean±SD.
987 Comparisons of parameters were performed with the 1-way (**E**) or 2-way (**H-L**)
988 ANOVA, followed by the Tukey honestly significant difference test for multiple
989 comparisons. ECs, endothelial cells; Nor, normoxia; Hyp, hypoxia; IgG,
990 immunoglobulin G; α-SMA, α-smooth muscle actin; COL1A1, collagen type I alpha 1;
991 FRET, fluorescence resonance energy transfer; CFP, cyan fluorescent protein; and YFP,
992 yellow fluorescent protein.

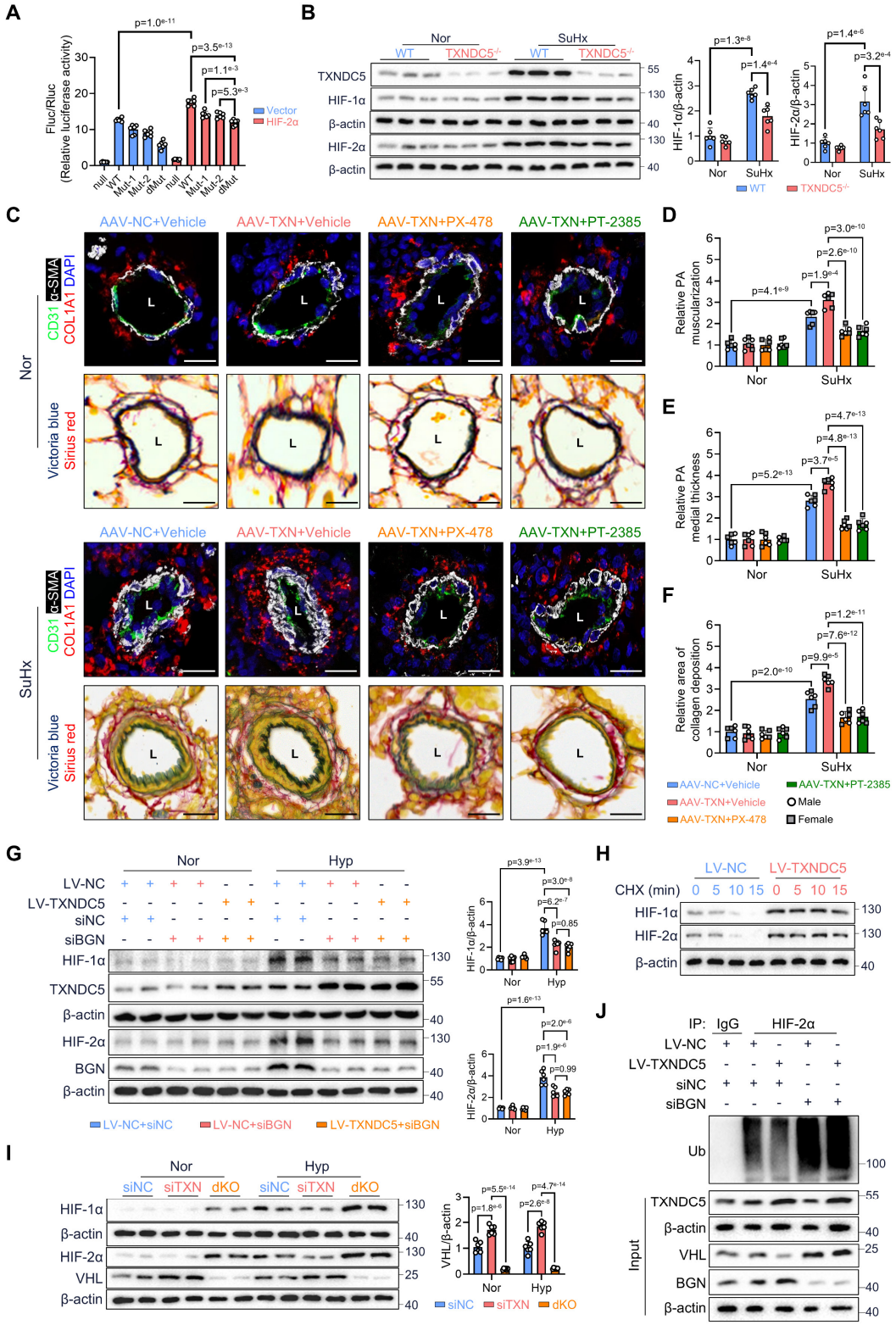

Figure 7. Endothelial TXNDC5 Driven PH via BGN-dependent stabilization of HIF-1α/2α.

A, Dual-luciferase assay showing that luciferase activity in constructs with BS1 mutation (Mut-1), BS2 mutation (Mut-2), or double mutation of BS1 and BS2 (dMut)

(n=6). **B**, Western blots showing the decreased protein levels of HIF-1α and HIF-2α in the lungs from TXNDC5 deficiency mice compared with WT exposed to SuHx (n=6). **C**, Representative distal pulmonary arteries (PAs) images from AAV-NC or AAV-TXN-treated mice exposed to SuHx or normoxia, with HIF-1α inhibitor (PX-478) or HIF-2α inhibitor (PT-2385), or vehicle administration. Multiplex immunohistochemical (mIF) showing CD31 (green), α-SMA (white), and COL1A1 (red) and Victoria blue/Sirius red (VB/SR) staining of elastic lamina (dark blue), perivascular collagens (red), and muscle fiber (yellow). Nuclei were counterstained with DAPI (blue). L indicates lumen. Scale bars=25 μm. **D**, **E**, and **F**, Quantitative analysis of distal PA remodeling, including PA muscularization assessed by α-SMA-positive area (n=6), medial wall thickness measured across the elastic lamina visualized by VB staining (n=6), and perivascular collagen area quantified using SR staining (n=6). **G**, Representative Western blots showing that the LV-TXNDC5-induced upregulation of HIF-1/2α was abolished by siBGN in hPAECs both under normoxia and hypoxia conditions (n=6). **H**, Western blot showing that the protein stabilization of HIF-1/2α was enhanced by LV-TXNDC5 treatment in hPAECs under normoxic conditions (n=5). **I**, Representative Western blots of HIF-1α, HIF-2α, and VHL in hPAECs after treatment with TXNDC5 knockdown only or double knockdown (dKO) of TXNDC5 and VHL (n=6). **J**, Western blot analysis indicating the HIF-2α ubiquitylation profile was reduced by LV-TXNDC5 but increased by siBGN treatment. hPAECs were treated with 10 μM MG132 for 6 h before harvest. Data represent the mean±SD. Comparisons of parameters were performed with 2-way ANOVA, followed by the Tukey honestly significant difference test for multiple comparisons. BS indicates binding site; VHL, von Hippel-Lindau; Ub, ubiquitin; Nor, normoxia; Hyp, hypoxia; SuHx, Sugen5416/hypixa; IgG, immunoglobulin G; LV, lentivirus; α-SMA, α-smooth muscle actin; and COL1A1, collagen type I alpha 1.

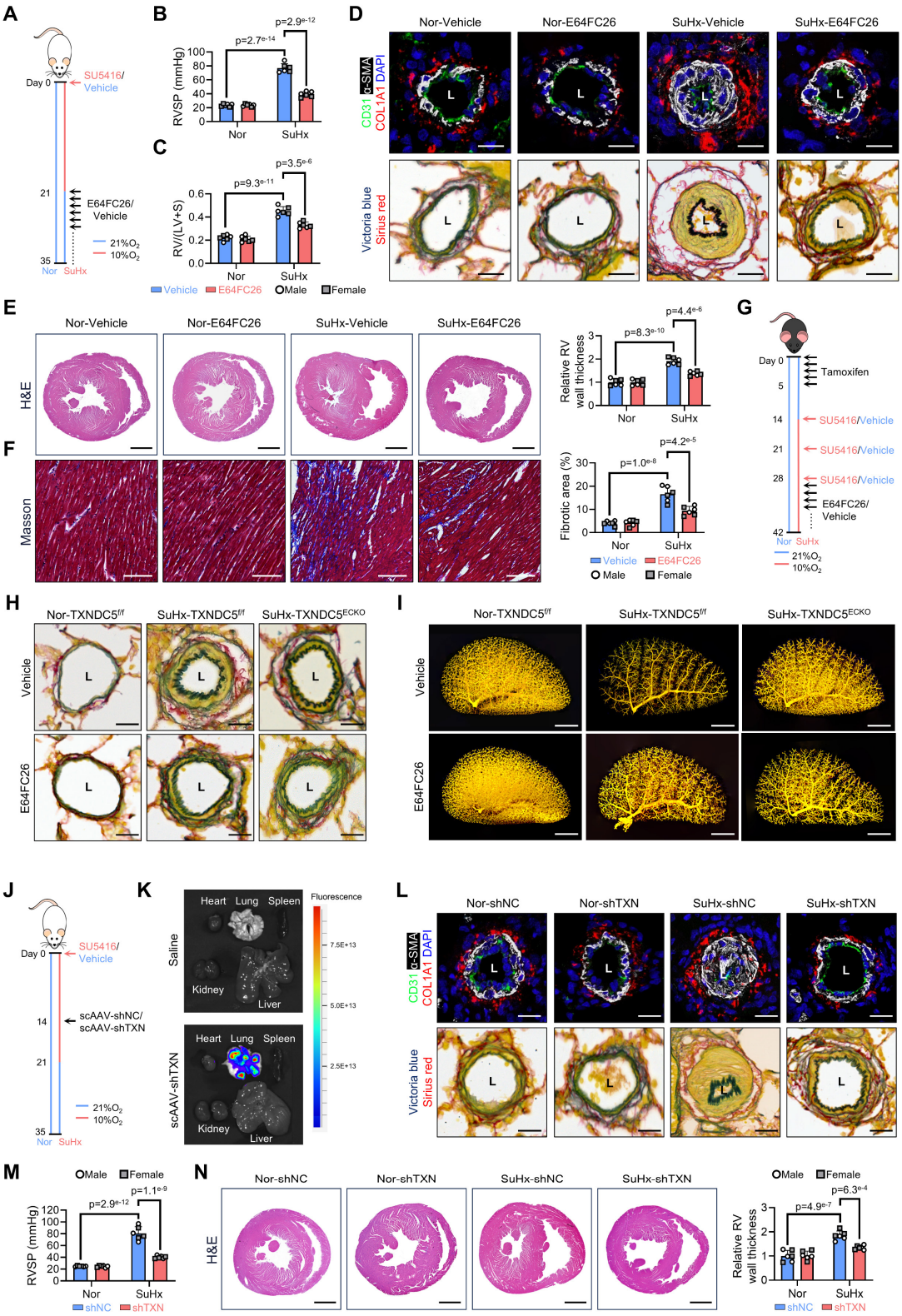

Figure 8. Pharmacological and Pulmonary Endothelium-Targeted Inhibition of TXNDC5 Ameliorated PH.

A, Schematic protocol for E64FC26 administration for SuHx-induced PH rats. Rats were treated with SuHx for 3 weeks and then intraperitoneal injection with 2 mg/kg

1028 E64FC26 daily for 2 weeks under normoxic conditions. **B**, Quantification of right
1029 ventricular systolic pressure (RVSP) in rats administered with E64FC26 or vehicle
1030 exposed to normoxia or SuHx (n=6). **C**, Fulton index [RV/(LV+S)] of rats with
1031 E64FC26 or vehicle treatment under normoxia or SuHx conditions (n=6). **D**,
1032 Representative multiplex immunofluorescence (mIF) of distal pulmonary arteries (PAs)
1033 from rats treated with vehicle or E64FC26 under normoxia or SuHx conditions,
1034 showing CD31 (green), α-SMA (white), and COL1A1 (red), together with Victoria
1035 blue/Sirius red (VB/SR) staining of elastic lamina (dark blue), perivascular collagens
1036 (red), and muscle fiber (yellow). Nuclei were counterstained with DAPI (blue). L
1037 indicates lumen. Scale bars = 25 μm. **E**, Histological and quantification analysis of the
1038 cross-sectioned heart at the mid-RV plane (top) and the highlighted right ventricular
1039 wall (bottom) of rats treated with E64FC26 or vehicle under normoxia or SuHx
1040 conditions (n=6). Scale bars=2 mm. **F**, Masson's trichrome staining and quantification
1041 of the fibrotic area by collagen volume fraction measured by Image J of RV from rats
1042 treated with E64FC26 or vehicle exposed to normoxia or SuHx (n=6). Scale bars=100
1043 μm. **G**, Schematic of vehicle or E64FC26 treatment in $TXNDC5^{f/f}$ and $TXNDC5^{ECKO}$
1044 mice under SuHx conditions to investigate whether the effects of E64FC26 are
1045 TXNDC5-dependent. **H**, Representative distal PAs images from $TXNDC5^{f/f}$ and
1046 $TXNDC5^{ECKO}$ mice treated with vehicle or E64FC26 under SuHx or normoxia
1047 conditions. Victoria blue/Sirius red (VB/SR) staining of elastic lamina (dark blue),
1048 perivascular collagens (red), and muscle fiber (yellow). L indicates lumen. Scale
1049 bars=25 μm. **I**, Representative lung angiogram of SuHx-treated $TXNDC5^{f/f}$ and
1050 $TXNDC5^{ECKO}$ mice with or without E64FC26 administration, showing distal
1051 pulmonary perfusion. Scale bars=2 mm. **J**, Schematic diagram of the pulmonary
1052 endothelium-targeted gene therapy strategy. Rats received a tail vein injection of self-
1053 complementary adeno-associated virus (scAAV) encoding shRNA against TXNDC5
1054 (shTXN) or control shRNA (shNC). **K**, Representative IVIS images of major organs
1055 from rats treated with Saline or scAAV-shTXN, showing GFP fluorescence delivered
1056 by the scAAV vector. **L**, Representative mIF for CD31 (green), α-SMA (white), and
1057 COL1A1 (red), and VB/SR staining for elastic lamina (dark blue), collagens (red), and

muscle fiber (yellow) in distal PAs from rats receiving shNC or shTXN exposed to normoxia or SuHx. Nuclei were counterstained with DAPI (blue). L indicates lumen. Scale bars=25 μm. **M**, Hemodynamic measurement of RVSP in SuHx-induced PH rats treated with shNC or shTXN (n=6). **N**, Histological sections of the heart at the mid-RV plane and quantification of right ventricular wall thickness from SuHx-induced PH rats treated with shNC or shTXN (n=6). Scale bars = 2 mm. Data represent the mean±SD. Comparisons of parameters were performed with 2-way ANOVA, followed by Tukey honestly significant difference test for multiple comparisons. H&E indicates hematoxylin-eosin; α-SMA, α-smooth muscle actin; COL1A1, collagen type I alpha 1; shRNA, short hairpin RNA; f/f, flox/flox; Nor, normoxia; SuHx, Sugen5416/hypoxia; and RV, right ventricle.

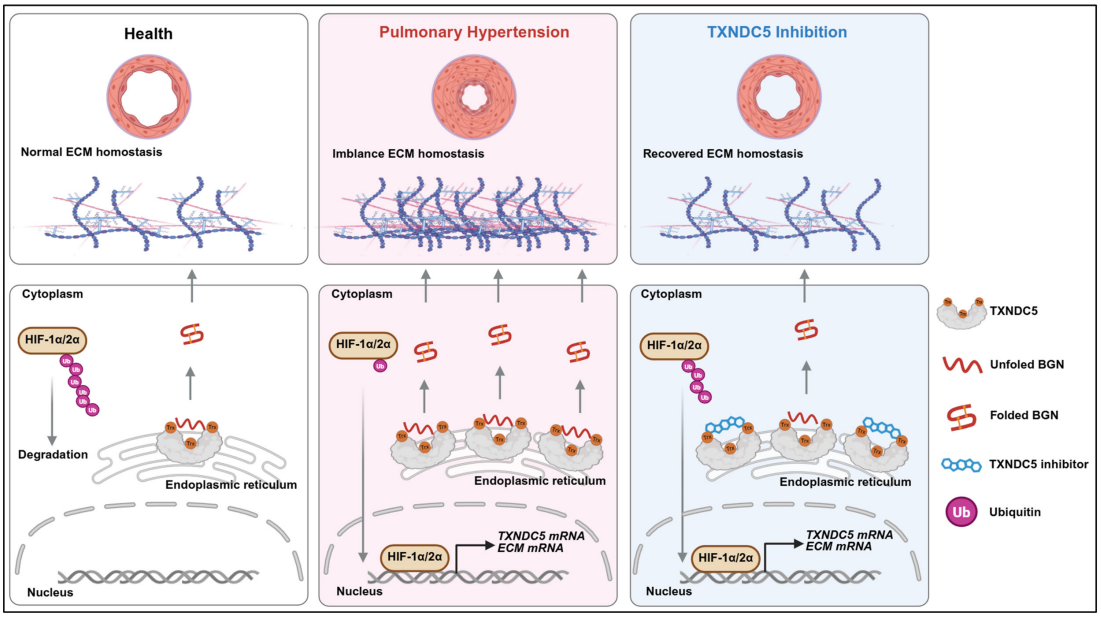

Graphic Abstract. The role of TXNDC5 in regulating ECM homeostasis during PH. In the healthy state, BGN folding is properly maintained and HIF-1α/2α is rapidly degraded. During PH, TXNDC5 is upregulated, leading to excessive accumulation of BGN and impaired ubiquitination-mediated degradation of HIF-1α/2α, resulting in an imbalance in ECM homeostasis and contributing to vascular remodeling. Pharmacological or genetic inhibition of TXNDC5 restores BGN folding capacity and facilitates HIF-1α/2α degradation, thereby reestablishing ECM homeostasis and

1078 attenuating PH progression.

1079

Supplemental Figures

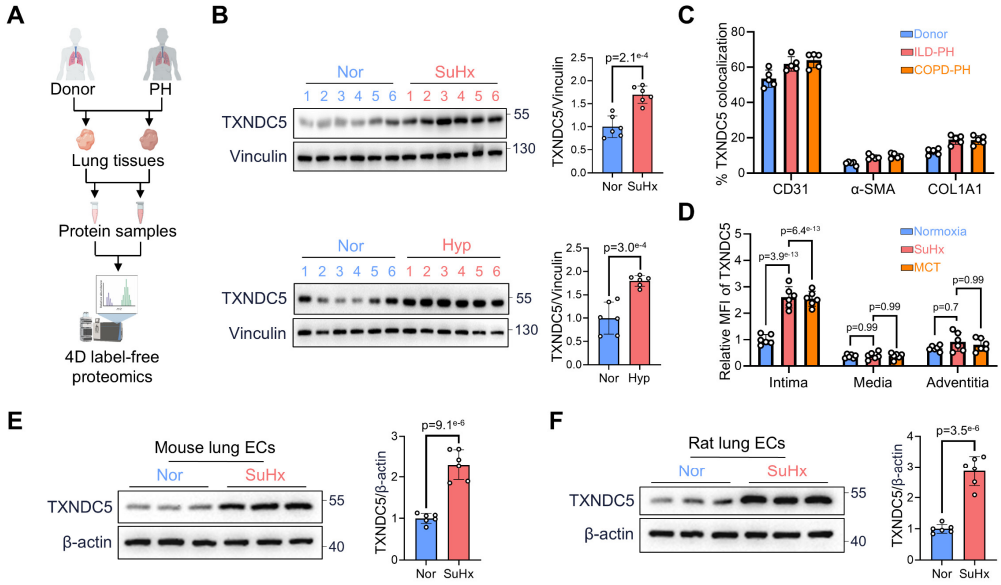

Figure S1. Upregulation of TXNDC5 in the lungs and lung endothelial cells of PH rodent models.

A, Schematic illustration showing the 4D label-free proteomics of lungs from non-PH donors and patients with hypoxic PH. **B**, Western blot analysis and quantification of TXNDC5 and Vinculin in the lungs of mice exposed to SuHx or hypoxia or under normoxic situations (n=6). **C**, Quantitative analysis of mIF showing TXNDC5 was predominantly co-localized with CD31 in distal PAs. (n=5). **D**, Quantification of mean fluorescence intensity (MFI) of TXNDC5 in remodeled distal PAs from SuHx- and MCT-induced rat PH models compared with rats under normoxic conditions. (n=6). **E**, Western blot of TXNDC5 in primary lung ECs from SuHx-induced mice or normoxic controls, showing increased protein levels in ECs. **F**, Western blot of TXNDC5 in lung ECs isolated from SuHx-induced PH rats, demonstrating elevated expression compared with normoxic controls. Data represent the mean±SD. Comparisons of parameters were performed with the unpaired 2-tailed Student *t*-test (**B**, **E**, and **F**) or 2-way ANOVA (**D**), followed by Tukey honestly significant difference test for multiple comparisons. Nor indicates normoxia; Hyp, hypoxia; SuHx, Sugen5416/hypoxia; and ECs, endothelial cells.

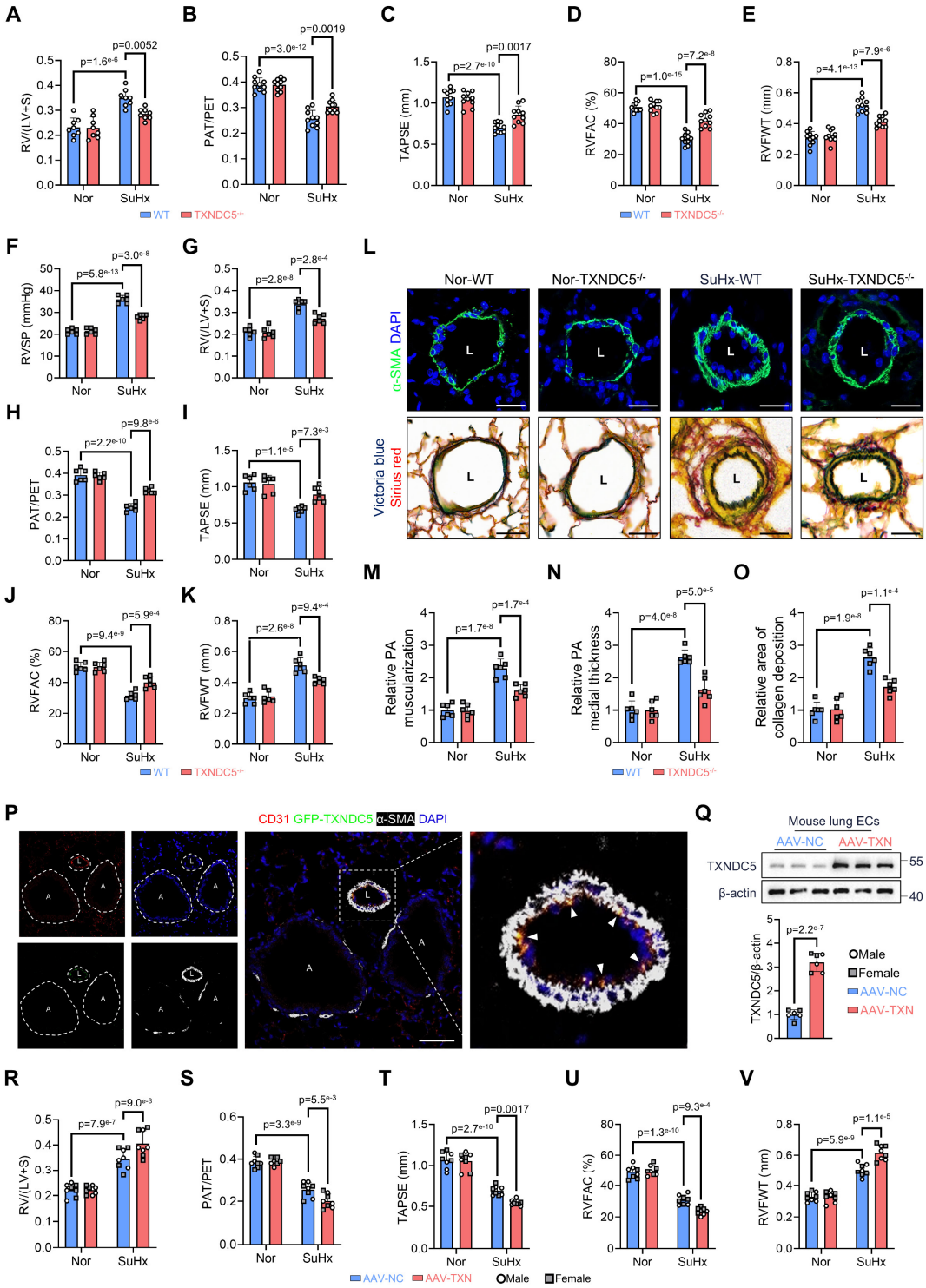

Figure S2. Role of TXNDC5 in PH development.

A, Fulton index [RV/(LV+S)] in male WT and TXNDC5$^{-/-}$ mice exposed to normoxia or SuHx (n=8). **B**, **C**, **D**, and **E**, Echocardiography analysis of PAT/PET, TAPSE, RVFAC, and RVFWT in male WT and TXNDC5$^{-/-}$ mice exposed to normoxia or SuHx (n=10). **F**, Right ventricular systolic pressure (RVSP) in female WT and TXNDC5$^{-/-}$

1106 mice under normoxia or SuHx (n=6). **G**, RV/(LV+S) in female WT and TXNDC5$^{-/-}$
1107 mice (n=6). **H**, **I**, **J,** and **K**, Echocardiographic assessment of right ventricular function
1108 of female WT and TXNDC5$^{-/-}$ mice, including PAT/PET, TAPSE, RVFAC, and RVFWT
1109 (n=6). **L**, Representative images of distal PAs from female WT and TXNDC5$^{-/-}$ mice
1110 under normoxia or SuHx conditions, showing α-SMA immunofluorescence (green) and
1111 Victoria blue/Sirius red (VB/SR) staining of elastic lamina (dark blue), perivascular
1112 collagens (red), and muscle fiber (yellow). Nuclei were counterstained with DAPI
1113 (blue). L indicates lumen. Scale bars=25 μm. **M**, **N,** and **O**, Quantification of distal PA
1114 remodeling in female WT and TXNDC5$^{-/-}$mice, including PA muscularization, medial
1115 wall thickness, and collagen deposition area (n=6). **P**, Representative confocal images
1116 showing GFP-TXNDC5 (green), CD31 (red), and α-SMA (white) in lung sections from
1117 AAV-TXN-treated mice. Nuclei were counterstained with DAPI (blue). L indicates
1118 lumen. A indicates airway. Scale bars=50 μm. **Q**, Western blot analysis of TXNDC5
1119 protein levels in primary lung ECs isolated from AAV-TXN- or AAV-NC-treated mice
1120 (n=6). **R**, RV/(LV+S) in male and female mice administered with AAV-NC or AAV-
1121 TXN exposed to normoxia or SuHx (n=8). **S**, **T**, **U**, and **V**, Echocardiography analysis
1122 of PAT/PET, TAPSE, RVFAC, and RVFWT in both male and female mice administered
1123 with AAV-NC or AAV-TXN exposed to normoxia or SuHx (n=8). Data represent the
1124 mean±SD. Comparisons of parameters were performed with the unpaired 2-tailed
1125 Student *t*-test (**Q**) or 2-way ANOVA (**A-K**, **M-O,** and **R-V**), followed by Tukey
1126 honestly significant difference test for multiple comparisons. Nor indicates normoxia;
1127 SuHx, Sugen5416/hypoxia; PAT/PET, pulmonary artery acceleration time/pulmonary
1128 artery ejection time ratio; TAPSE, tricuspid annular plane systolic excursion; RVFAC,
1129 right ventricular fractional area change; and RVFWT, right ventricular free wall
1130 thickness.

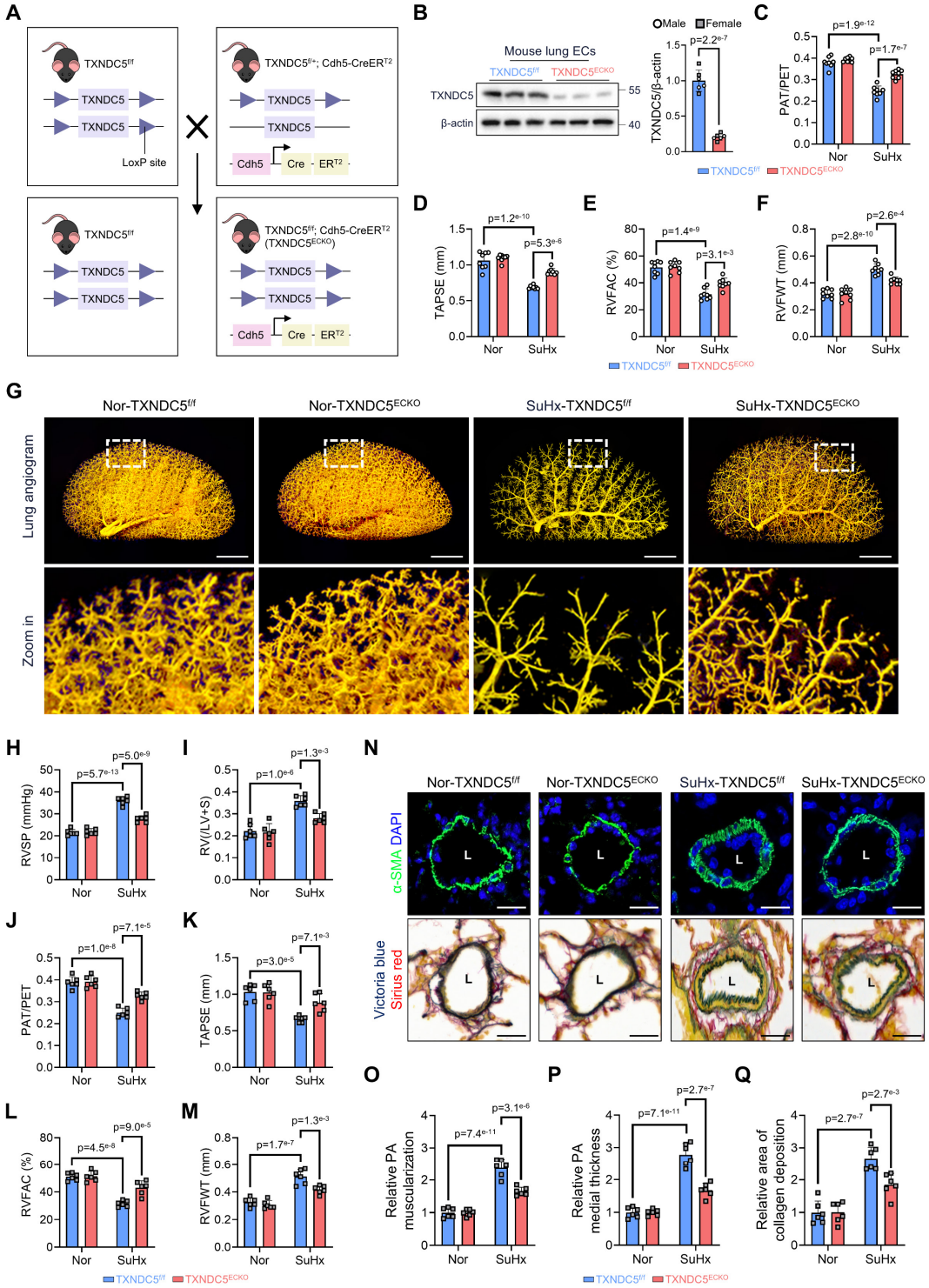

Figure S3. Protective effects of endothelial cell-specific TXNDC5 deletion on SuHx-induced PH.

A, Schematic illustrating the generation of endothelial cell-specific TXNDC5 knockout ($TXNDC5^{ECKO}$) mice. **B**, Representative Western blots and quantification of TXNDC5 protein levels in primary lung ECs isolated from $TXNDC5^{f/f}$ and $TXNDC5^{ECKO}$ mice

(n=6). **C**, **D**, **E**, and **F**, Echocardiographic assessment of right ventricular function in male TXNDC5$^{f/f}$ and TXNDC5^{ECKO} under normoxia or SuHx, including PAT/PET, TAPSE, RVFAC, and RVFWT (n=6). **G**, Enlarged lung angiogram images of the left lungs from TXNDC5$^{f/f}$ and TXNDC5^{ECKO} mice treated with SuHx or under normoxic conditions. Scale bars=2 mm. **H**, Right ventricular systolic pressure (RVSP) in female TXNDC5$^{f/f}$ and TXNDC5^{ECKO} under normoxia or SuHx (n=6). **I**, Fulton index [RV/(LV+S)] in female TXNDC5$^{f/f}$ and TXNDC5^{ECKO} mice (n=6). **J**, **K**, **L,** and **M**, Echocardiographic evaluation of right ventricular function in female TXNDC5^{ECKO} and littermate control mice, including PAT/PET, TAPSE, RVFAC, and RVFWT (n=6). **N**, Representative distal PA images from female TXNDC5$^{f/f}$ and TXNDC5^{ECKO} exposed to normoxia or SuHx, showing α-SMA (green) and VB/SR staining of elastic lamina (dark blue), collagens (red), and muscle fiber (yellow). Nuclei stained with DAPI (blue). L indicates lumen. Scale bars=25 μm. **O**, **P**, and **Q**, Quantitative analysis of distal PA remodeling in female TXNDC5$^{f/f}$ and TXNDC5^{ECKO} mice, including PA muscularization, medial wall thickness, and collagen deposition (n=6). Data represent the mean±SD. Comparisons of parameters were performed with the unpaired 2-tailed Student *t*-test (**B**) or 2-way ANOVA (**C**-**F**, **H-M,** and **O-Q**), followed by Tukey honestly significant difference test for multiple comparisons. DAPI indicates 4′,6-diamidino-2-phenylindole; α-SMA, α-smooth muscle actin; f/f, flox/flox; Nor, normoxia; SuHx, Sugen5416/hypoxia; PAT/PET, pulmonary artery acceleration time/pulmonary artery ejection time ratio; TAPSE, tricuspid annular plane systolic excursion; RVFAC, right ventricular fractional area change; and RVFWT, right ventricular free wall thickness.

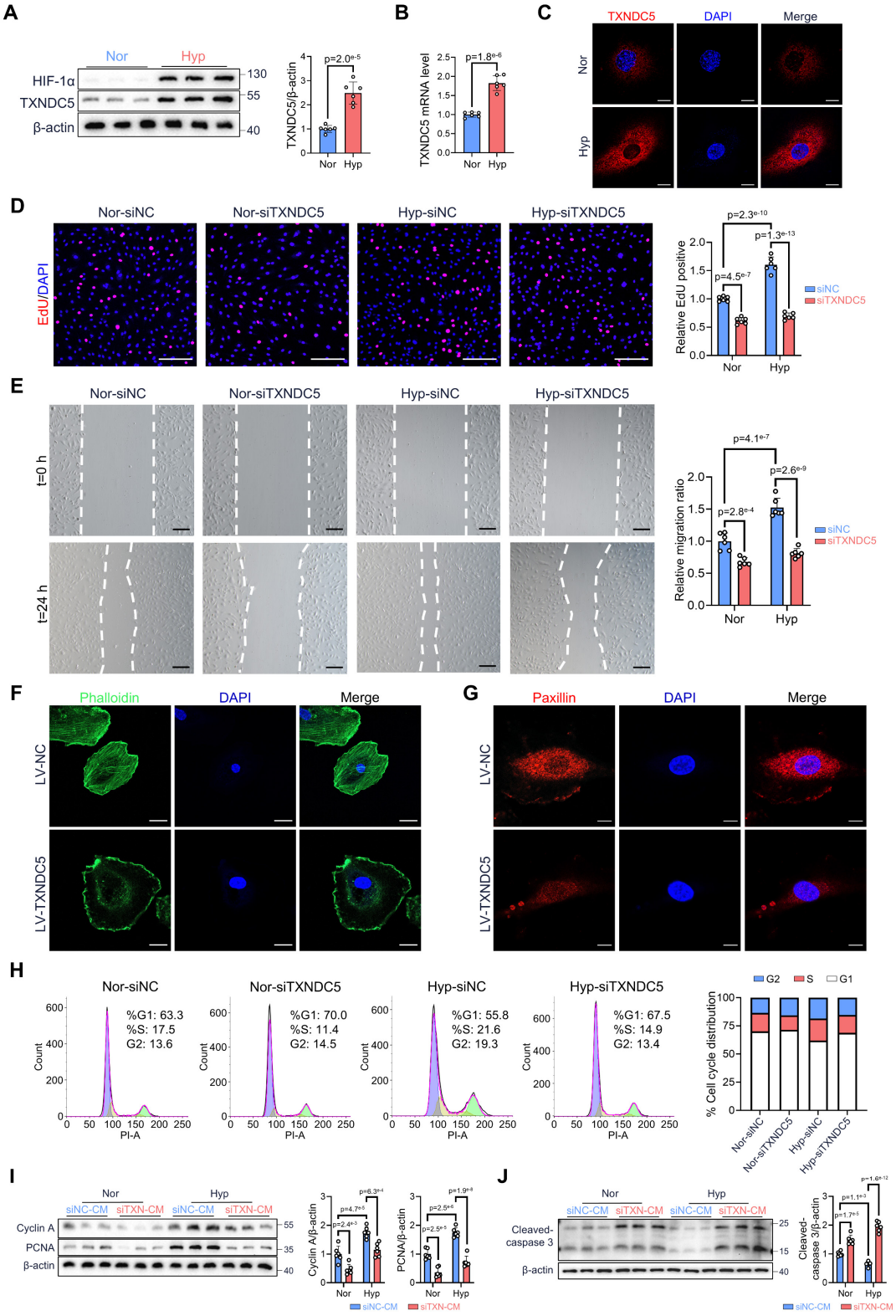

Figure S4. TXNDC5 regulated cell function in pulmonary artery.

A and **B**, Quantification of TXNDC5 protein levels by Western blots and TXNDC5 mRNA levels by qPCR analysis in hPAECs in both normoxia and hypoxia situations (n=6). **C**, Immunofluorescence staining analysis showing increased protein levels of

1164 TXNDC5 exposed to hypoxia. Scale bars=10 μm. **D**, Representative EdU (red) staining
1165 image and group data showing the effects of TXNDC5 silencing on the proliferative
1166 activity of hPAECs (n=6). Nuclei were counterstained with DAPI (blue). Scale
1167 bars=200 μm. **E**, Representative images and group data showing the migration of
1168 hPAECs treated with hPAECs siTXNDC5 or siNC in normoxia or hypoxia conditions
1169 (n=6). Scale bars=200 μm. **F** and **G**, Confocal microscopy images showing the effect
1170 of LV-TXNDC5 on the cytoskeletal architecture of hPAECs. Cells were stained with
1171 phalloidin (green, scale bars=20 μm) or paxillin (red, scale bars=10 μm). Nuclei were
1172 counterstained with DAPI (blue). **H**, Flow cytometry showing the effect of siTXNDC5
1173 on the cell cycle of hPAECs exposed to normoxia or hypoxia. The representative
1174 images and quantification of percentages of cells in G1, S, and G2 were shown (n=6).
1175 X and Y axes, respectively, indicate the denoted DNA content stained with propidium
1176 iodide (PI) and cell counts. **I** and **J**, Representative Western blots and quantification
1177 showing the protein levels of Cyclin A, proliferating cell nuclear antigen (PCNA), and
1178 cleaved-caspase 3 of hPASMCs treated with conditioned medium from hPAECs
1179 transfected with siTXNDC5 or siNC in normoxia or hypoxia conditions (n=6). Data
1180 represent the mean±SD. Comparisons of parameters were performed with the unpaired
1181 2-tailed Student *t*-test (**A** and **B**) or 2-way ANOVA (**D**, **E**, **I**, and **J**), followed by Tukey
1182 honestly significant difference test for multiple comparisons. Nor indicates normoxia;
1183 Hyp, hypoxia; LV, lentivirus; si, small interfering; CM, conditioned medium; and EdU,
1184 5-ethynyl-20-deoxyuridine.

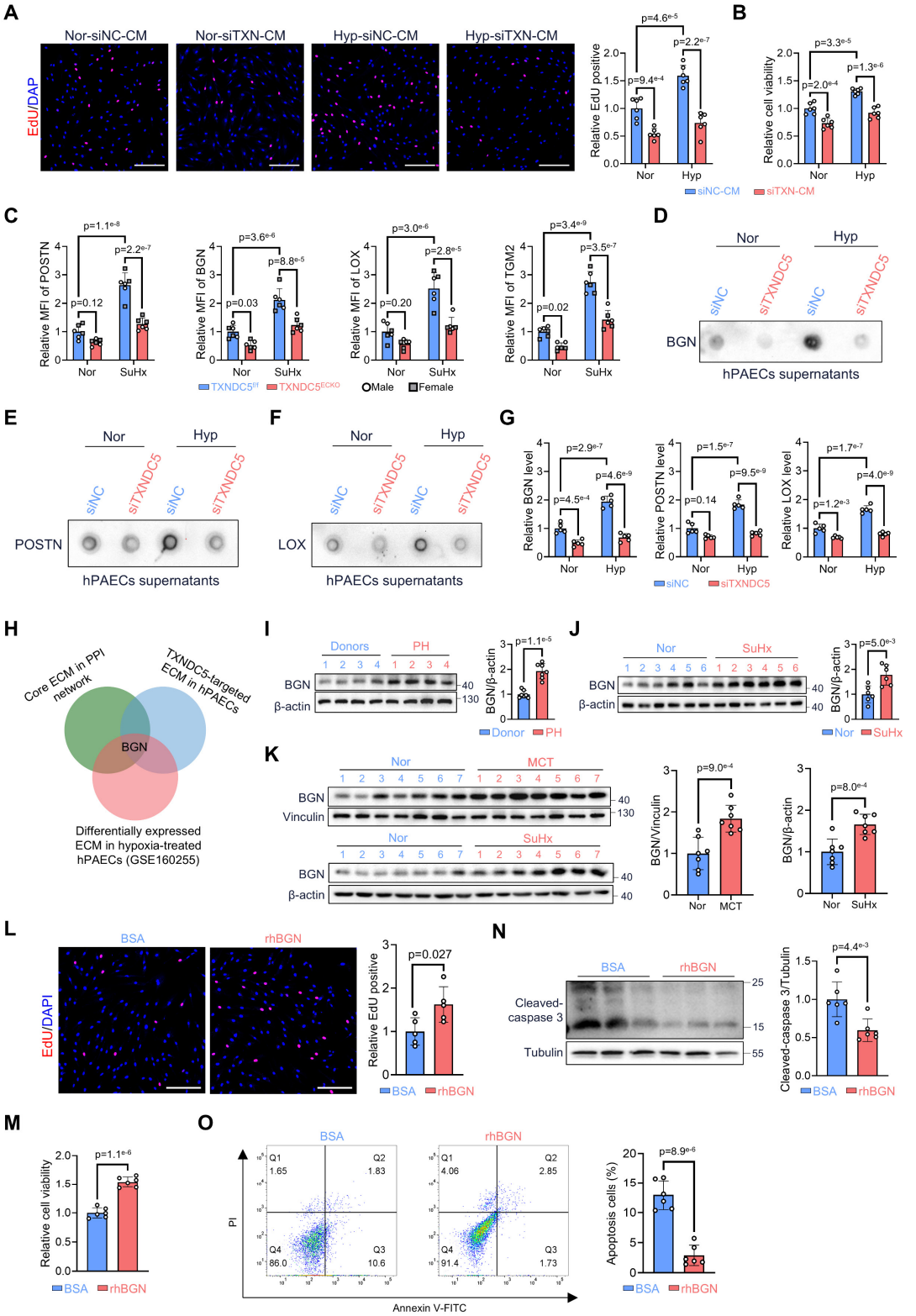

Figure S5. TXNDC5-driven endothelial paracrine signaling and ECM remodeling. **A**, Representative EdU staining image and group data showing the proliferative activity of hPASMCs treated with conditioned medium from hPAECs transfected with siTXNDC5 (siTXN-CM) or siNC (siNC-CM) in normoxia or hypoxia conditions (n=6).

1190 Nuclei were counterstained with DAPI (blue). Scale bars=200 μm. **B**, CCK-8 assays
1191 demonstrating decreased cell viability of hPASMCs after treatment with siTXN-CM or
1192 siNC-CM (n=6). **C**, Quantification of POSTN, BGN, LOX, and TGM2 deposition in
1193 distal PAs from SuHx-treated TXNDC5$^{f/f}$ and TXNDC5^{ECKO} mice, assessed by mean
1194 fluorescence intensity (MFI) (n=6). **D**, **E**, and **F**, Representative dot blot analysis of
1195 BGN, POSTN, and LOX in the supernatants of hPAECs transfected with siTXNDC5
1196 or control siRNA (siNC). **G**, Quantification of dot blot intensities for BGN, POSTN,
1197 and LOX, showing significantly reduced secretion upon TXNDC5 knockdown in
1198 normoxia or hypoxia conditions (n=5). **H**, Venn diagram showing that BGN exists in
1199 the overlapping of the core ECM genes in the PPI network, the differentially expressed
1200 ECM proteins in TXNDC5 silencing hPAECs, and the differentially expressed ECM
1201 genes in hypoxia-treated hPAECs (GSE160255). **I**, Representative Western blots and
1202 quantification of BGN and vinculin in the lungs of donors and PH patients (n=7). **J**,
1203 Representative Western blots and quantification of BGN and β-actin in the lungs from
1204 mice exposed to SuHx or under normoxic conditions (n=6). **K**, Western blots showing
1205 the BGN protein levels in the lungs collected from MCT or SuHx-treated rats or rats
1206 under normoxia (n=7). **L**, Representative EdU staining image and group data showing
1207 10 μg/ml recombinant human biglycan (rhBGN) treatment for 24 h enhanced the
1208 proliferative activity of hPASMCs (n=5). Scale bars=200 μm. **M**, CCK-8 assay
1209 confirming increased cell viability of hPASMCs after rhBGN treatment (n=6). **N**,
1210 Western blots showing the protein levels of cleaved-caspase 3 of hPASMCs treated with
1211 10 μg/ml rhBGN or the negative control (bovine serum albumin, BSA) for 24 h (n=6).
1212 **O**, Flow cytometry analysis of Annexin V-FITC/PI staining demonstrating decreased
1213 apoptotic cell populations in hPASMCs treated with rhBGN (n=6). Data represent the
1214 mean±SD. Comparisons of parameters were performed with the unpaired 2-tailed
1215 Student *t*-test (**I-O**) or 2-way ANOVA (**A-C** and **G**), followed by Tukey honestly
1216 significant difference test for multiple comparisons. Nor indicates normoxia; Hyp,
1217 hypoxia; SuHx, Sugen5416/hypoxia; MCT, monocrotaline; si, small interfering; DAPI,
1218 4′,6-diamidino-2-phenylindole; f/f, flox/flox; POSTN, periostin; BGN, biglycan; and
1219 LOX, lysyl oxidase; TGM2, transglutaminase 2.

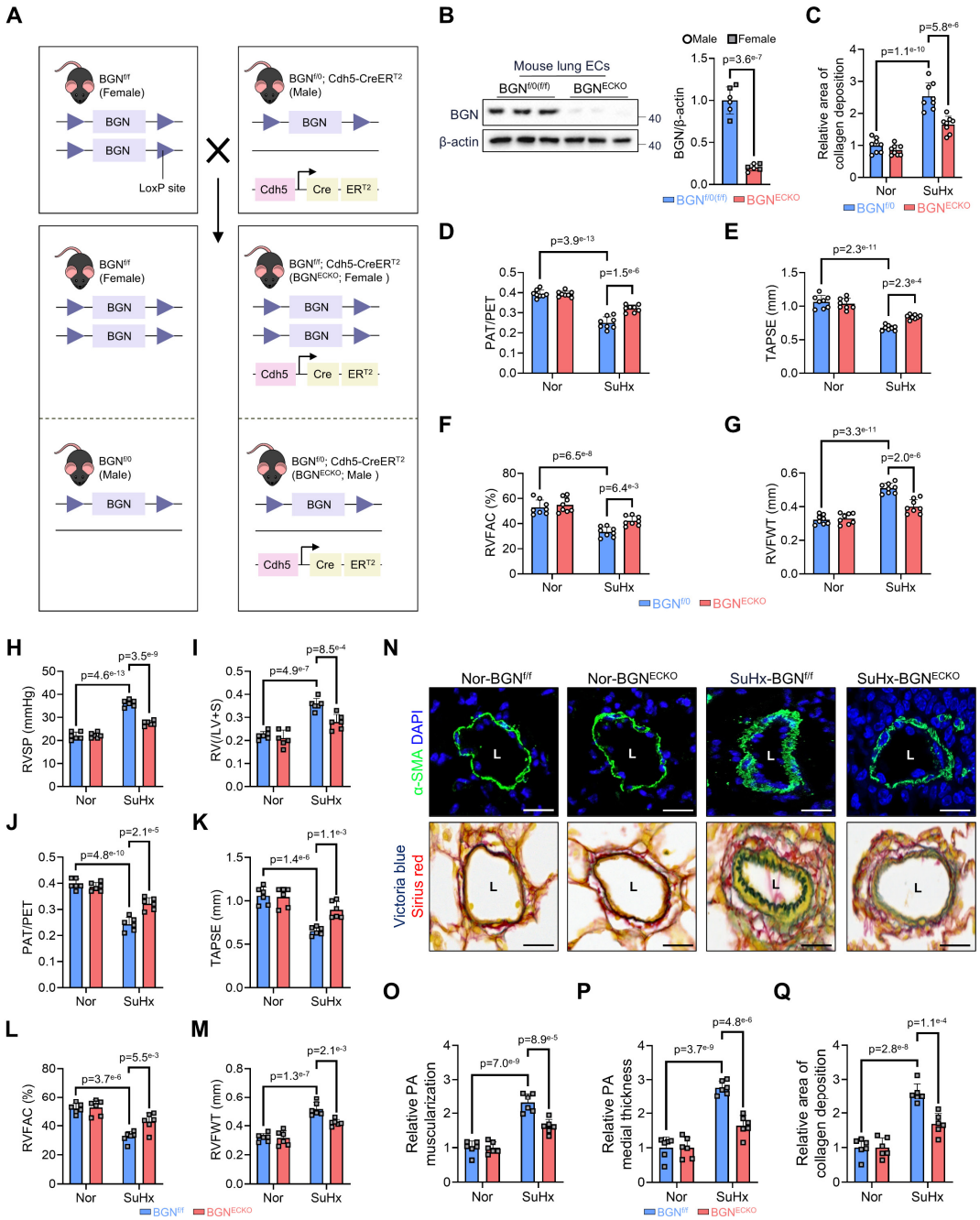

Figure S6. Endothelial BGN deficiency protected against pulmonary vascular remodeling and RV failure in PH.

A, Schematic illustrating the generation of endothelial cell-specific BGN knockout (BGN^{ECKO}) mice. As BGN is an X chromosome-located gene, male mice carry a single floxed allele ($BGN^{f/0}$), whereas female mice carry double floxed alleles ($BGN^{f/f}$). **B**, Representative Western blots and quantification of BGN protein levels in primary lung ECs isolated from $BGN^{f/0(f/f)}$ and BGN^{ECKO} mice (n=6). **C**, Quantification of collagen

deposition of distal pulmonary arteries (PAs) from male $BGN^{f/0}$ and BGN^{ECKO} mice under normoxia or SuHx(n=8). **D**, **E**, **F**, and **G**, Echocardiographic assessment of right ventricular function in male $BGN^{f/0}$ and BGN^{ECKO} under normoxia or SuHx, including PAT/PET, TAPSE, RVFAC, and RVFWT (n=8). **H**, Right ventricular systolic pressure (RVSP) in $BGN^{f/f}$ and female BGN^{ECKO} under normoxia or SuHx (n=6). **I**, Fulton index [RV/(LV+S)] in $BGN^{f/f}$ and BGN^{ECKO} mice (n=6). **J**, **K**, **L,** and **M**, Echocardiographic evaluation of PAT/PET, TAPSE, RVFAC, and RVFWT in female BGN^{ECKO} and littermate control mice (n=6). **N**, Representative distal PA images from $BGN^{f/f}$ and BGN^{ECKO} exposed to normoxia or SuHx, showing α-SMA (green) and VB/SR staining of elastic lamina (dark blue), collagens (red), and muscle fiber (yellow). Nuclei stained with DAPI (blue). L indicates lumen. Scale bars=25 μm. **O**, **P**, and **Q**, Quantitative analysis of distal PA remodeling in $BGN^{f/f}$ and female BGN^{ECKO} mice, including PA muscularization, medial wall thickness, and collagen deposition (n=6). Data represent the mean±SD. Comparisons of parameters were performed with the unpaired 2-tailed Student *t*-test (**B**) or 2-way ANOVA (**C-M,** and **O-Q**), followed by Tukey honestly significant difference test for multiple comparisons. DAPI indicates 4′,6-diamidino-2-phenylindole; α-SMA, α-smooth muscle actin; f/0, flox/0; f/f, flox/flox; Nor, normoxia; SuHx, Sugen5416/hypoxia; PAT/PET, pulmonary artery acceleration time/pulmonary artery ejection time ratio; TAPSE, tricuspid annular plane systolic excursion; RVFAC, right ventricular fractional area change; and RVFWT, right ventricular free wall thickness.

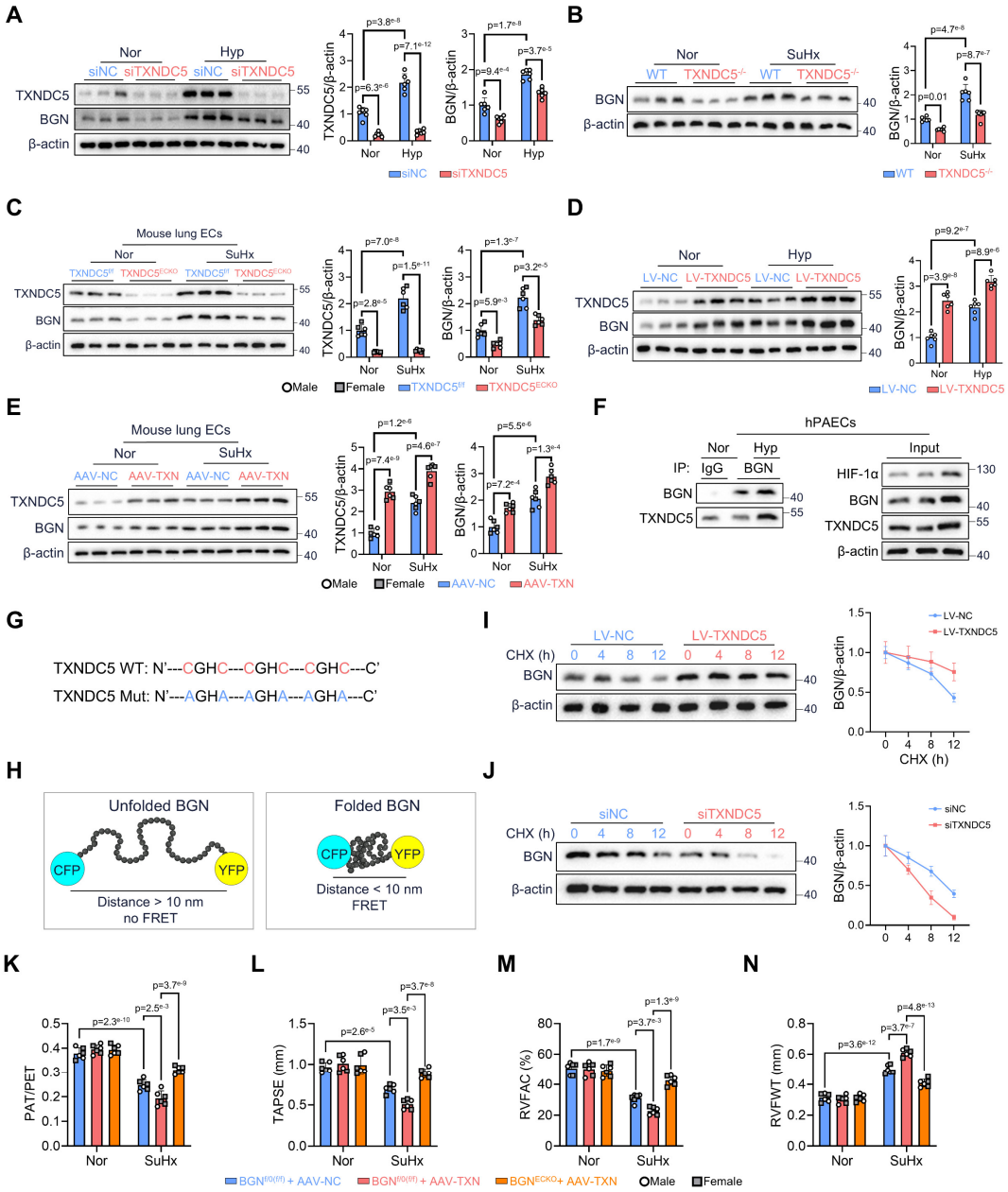

Figure S7. TXNDC5 stabilized BGN to regulate its protein expression.

A, Representative Western blots and quantification of TXNDC5 and BGN in hPAECs treated with siNC or siTXNDC5 under normoxia or hypoxia conditions (n=6). **B**, Western blot analysis showing the downregulation of BGN in the lungs from TXNDC5 deficiency mice compared with WT mice (n=6). **C**, Representative Western blots and quantification of TXNDC5 and BGN in lung ECs isolated from TXNDC5$^{f/f}$ and TXNDC5^{ECKO} mice under normoxia or SuHx conditions (n=6). **D**, Representative Western blots showing that the LV-TXNDC5-induced upregulation of BGN in hPAECs

both under normoxia and hypoxia conditions (n=6). **E**, Western blot analysis showing the upregulation of BGN in the lung ECs isolated from endothelial-specific AAV-NC or AAV-TXN-treated mice exposed to SuHx or under normoxic conditions (n=6). **F**, Coimmunoprecipitation analysis showing the interaction between TXNDC5 and BGN was enhanced by hypoxia stimulation in hPAECs. IP: BGN, immunoprecipitation with BGN antibody. IgG for the negative control. **G**, Scheme of WT (TXNDC5 WT) and mutant TXNDC5 (TXNDC5 Mut) sequences with Cysteine (C)-to-Alanine (A) mutations in all three thioredoxin domains. **H**, Schematic illustration for using FRET to determine the extent of BGN protein folding in hPAECs. When the BGN protein folds correctly (bottom), the distance between CFP and YFP will be less than 10 nm, resulting in FRET occurring. **I**, Western blot showing that TXNDC5 overexpression prolonged the BGN protein half-life in hPAECs (n=6). **J**, Western blot analysis demonstrating that TXNDC5 silencing destabilized BGN in hPAECs, resulting in accelerated protein degradation (n=6). **K**, **L**, **M**, and **N**, Echocardiographic evaluation of right ventricular function in $BGN^{f/0(f/f)}$ and BGN^{ECKO} mice with AAV-NC or AAV-TXN treatment (n=6), including PAT/PET, TAPSE, RVFAC, and RVFWT (n=6). Data represent the mean±SD. Comparisons of parameters were performed with 2-way ANOVA, followed by the Tukey honestly significant difference test for multiple comparisons. Nor indicates normoxia; Hyp, hypoxia; SuHx, Sugen5416/hypoxia; IgG, immunoglobulin G; LV, lentivirus; WT, wild-type; Mut, mutation; CHX, cycloheximide; FRET, fluorescence resonance energy transfer; CFP, cyan fluorescent protein; and YFP, yellow fluorescent protein.

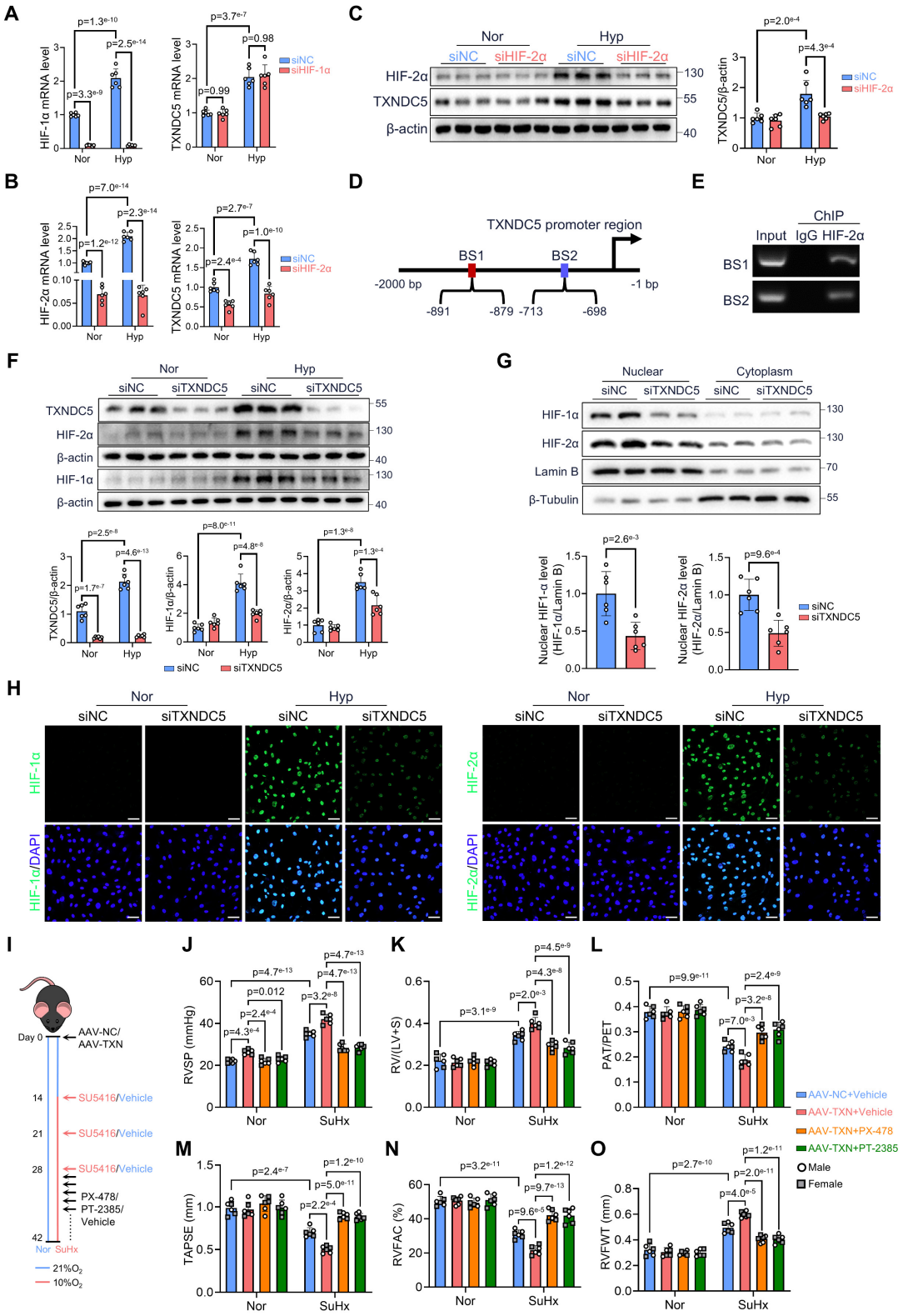

Figure S8. HIF signaling mediated TXNDC5-driven PH.

A and **B**, qPCR analysis showing the effects of HIF-1α (A) or HIF-2α (B) silencing on the mRNA expression of TXNDC5. Average expression values are normalized to the β-actin mRNA level. **C**, Western blot showing that siHIF-2α reduced the protein levels of

TXNDC5 in hPAECs under hypoxic conditions (n=6). **D**, Schematic illustration showing 2 sites in HIF-2α predicted to bind to the TXNDC5 promoter region. **E**, Chromatin immunoprecipitation (ChIP) followed by polymerase chain reaction analysis showing that the BS1 and BS2 regions are both for HIF-2α binding. **F**, Western blot analysis showing that silencing of TXNDC5 reduced the protein levels of HIF-1α and HIF-2α in hPAECs under hypoxic conditions (n=6). **G**, Western blots showing that siTXNDC5 reduced the protein levels of HIF-1α and HIF-2α in the nucleus exposed to hypoxia in hPAECs (n=6). **H**, Immunofluorescent staining analysis showing that siTXNDC5 reversed the increased levels of HIF-1α (green, left) or HIF-2α (green, right) induced by hypoxia in hPAECs. Nuclei were counterstained with DAPI (blue). Scale bars=50 μm. **I**. Schematic diagram of the pharmacological rescue experiment. AAV-NC or AAV-TXN was delivered via the tail vein to overexpress TXNDC5 in lung endothelial cells of mice, followed by normoxia or SuHx exposure, and then with HIF-1α inhibitor (PX-478) or HIF-2α inhibitor (PT-2385), or vehicle treatment. **J**. Hemodynamic measurements showing right ventricular systolic pressure (RVSP) in mice treated as described in (I) (n=6). **K**, Fulton index [RV/(LV+S)] of mice, assessing right ventricular hypertrophy (n=6). **L**, **M**, **N,** and **O**, Echocardiographic evaluation of right ventricular function, including PAT/PET, TAPSE, RVFAC, and RVFWT (n=6). Comparisons of parameters were performed with the unpaired 2-tailed Student *t*-test (**G**) or 2-way ANOVA (**A-C**, **F,** and **J-O**), followed by Tukey honestly significant difference test for multiple comparisons. BS indicates binding site; Nor, normoxia; Hyp, hypoxia; SuHx, Sugen5416/hypixa; ChIP, chromatin immune precipitation; PAT/PET, pulmonary artery acceleration time/pulmonary artery ejection time ratio; TAPSE, tricuspid annular plane systolic excursion; RVFAC, right ventricular fractional area change; and RVFWT, right ventricular free wall thickness.

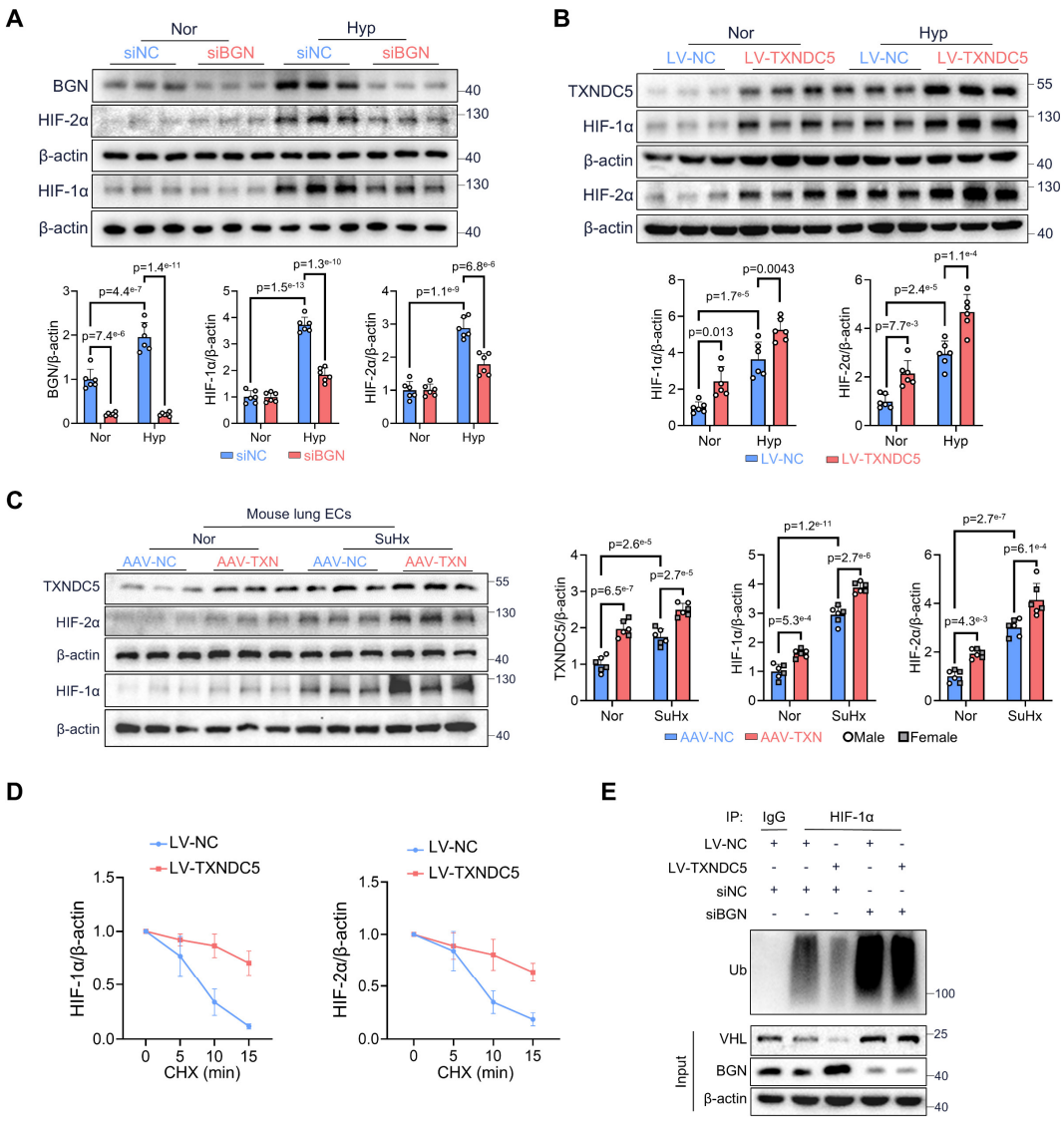

Figure S9. TXNDC5 inhibited the ubiquitination of HIF-1α/2α in a BGN-dependent manner.

A, Representative Western blots and quantification of BGN, and HIF-1/2α in hPAECs treated with siNC or siBGN under normoxia or hypoxia conditions (n=6). **B**, Western blot showing that the LV-TXNDC5-induced upregulation of HIF-1/2α in hPAECs both under normoxic and hypoxic situations (n=6). **C**, Representative Western blots and quantification of TXNDC5, HIF-1α, and HIF-2α in the lung ECs isolated from AAV-TXN or AAV-NC treated mice exposed to SuHx or under normoxic conditions (n=6). **D**, Quantification analysis showing that the protein half-life of endogenous HIF-1/2α was prolonged by LV-TXNDC5 treatment in hPAECs under normoxic conditions (n=5). **E**, Western blot analysis indicated that the HIF-1α ubiquitylation profile was reduced

by LV-TXNDC5 but increased by siBGN treatment. hPAECs were treated with 10 μM MG132 for 6 h before harvest. Data represent the mean±SD. Comparisons of parameters were performed with the 2-way ANOVA, followed by the Tukey honestly significant difference test for multiple comparisons. Nor indicates normoxia; Hyp, hypoxia; SuHx, Sugen5416/hypoxia; Ub, ubiquitin; IgG, immunoglobulin G; AAV, adeno-associated viruses; LV, lentivirus; and CHX, cycloheximide.

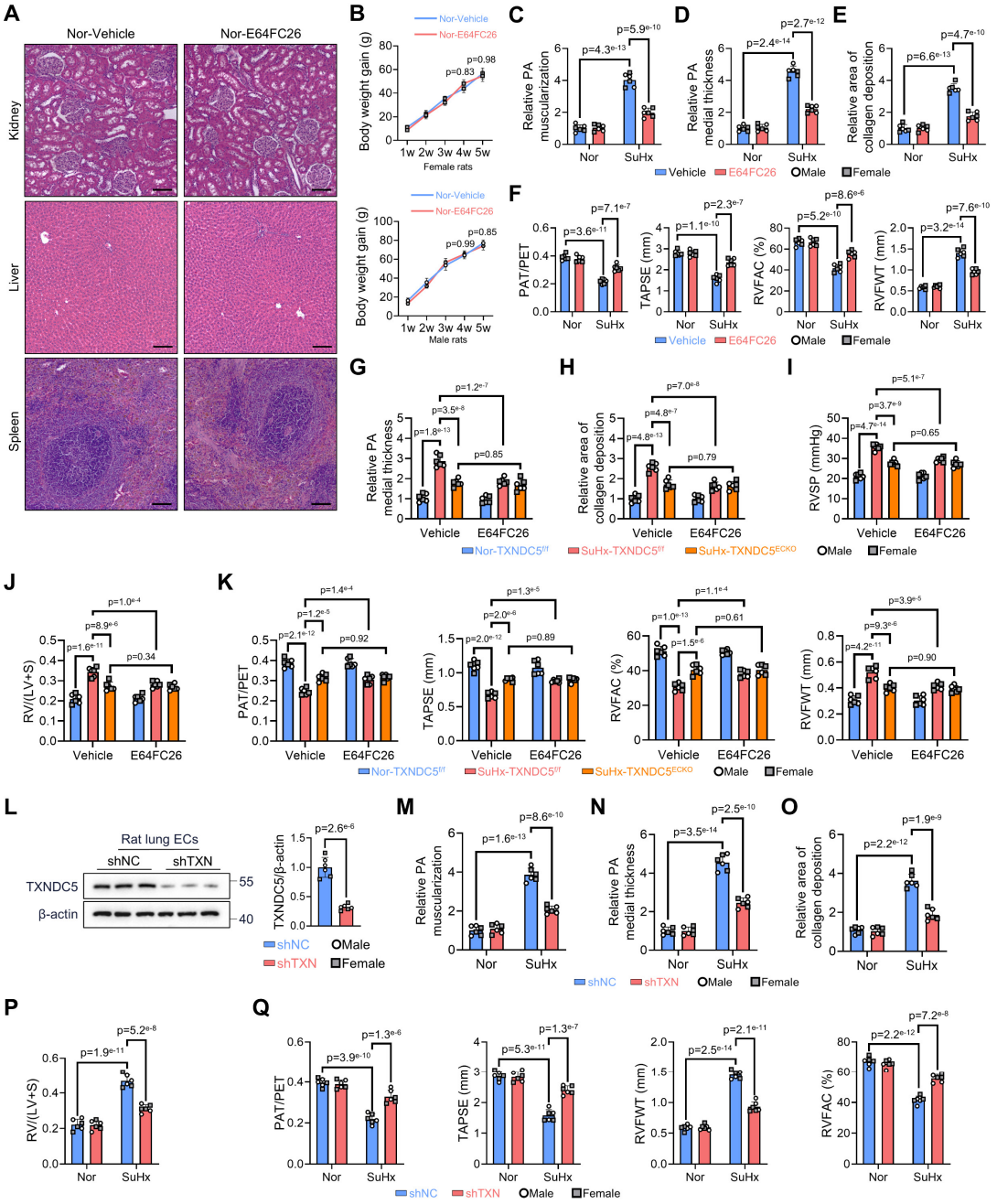

Figure S10. TXNDC5 inhibited the ubiquitination of HIF-1α/2α in a BGN-dependent manner.

A, Representative H&E staining of major kidney, liver, and spleen from rats maintained under normoxia for 5 weeks and continuously treated with E64FC26 or vehicle, showing preserved tissue morphology without apparent injury or inflammation. Scale bars=100 μm. **B**, Gain of body weight of female (top panel) and male (bottom panel) rats maintained under normoxia for 5 weeks with E64FC26 or vehicle treatment (n=6). **C**, **D**, and **E**, Quantification of distal pulmonary arteries (PAs) remodeling in SuHx-induced PH rats treated with vehicle or E64FC26, including distal PA muscularization, medial wall thickness, and collagen deposition area (n=6). **F**, Echocardiographic assessment of right ventricular function in rats with vehicle or E64FC26 treatment, including PAT/PET, TAPSE, RVFAC, and RVFWT (n=6). **G** and **H**, Quantification of distal PA medial wall thickness and collagen deposition area SuHx-treated $TXNDC5^{f/f}$ and $TXNDC5^{ECKO}$ mice with or without E64FC26 administration under SuHx or normoxia conditions (n=6). **I**, Right ventricular systolic pressure (RVSP) in $TXNDC5^{f/f}$ and $TXNDC5^{ECKO}$ mice treated with vehicle or E64FC26 (n=6). **J**, Fulton index [RV/(LV+S)] of $TXNDC5^{f/f}$ and $TXNDC5^{ECKO}$ mice with vehicle or E64FC26 treatment (n=6). **K**, Echocardiographic assessment of right ventricular function in $TXNDC5^{f/f}$ and $TXNDC5^{ECKO}$ mice treated with vehicle or E64FC26 exposed to SuHx or normoxia, including PAT/PET, TAPSE, RVFAC, and RVFWT (n=6). **L**, Western blot showing efficient knockdown of TXNDC5 in lung ECs isolated from rats receiving pulmonary endothelium-targeted self-complementary adeno-associated virus (scAAV) carrying shRNA against TXNDC5 (shTXN) compared with control shRNA (shNC) (n=6). **M**, **N**, and **O**, Quantification of distal PA remodeling in SuHx-induced PH rats treated with shNC or shTXN, including distal PA muscularization, medial wall thickness, and perivascular collagen deposition area (n=6). **P**, Fulton index [RV/(LV+S)] in rats treated with shNC or shTXN under normoxia or SuHx conditions (n=6). **Q**, Echocardiographic assessment of right ventricular function in rats receiving shNC or shTXN, including PAT/PET, TAPSE, RVFAC, and RVFWT (n=6). Data represent the mean±SD. Comparisons of parameters were performed with the unpaired 2-tailed Student *t*-test (**L**) or 2-way ANOVA (**B**-**K**, and **M-Q**), followed by Tukey honestly significant difference test for multiple comparisons. H&E indicates hematoxylin-eosin;

f/f, flox/flox; Nor, normoxia; SuHx, Sugen5416/hypoxia; shRNA, short hairpin RNA; PAT/PET, pulmonary artery acceleration time/pulmonary artery ejection time ratio; TAPSE, tricuspid annular plane systolic excursion; RVFAC, right ventricular fractional area change; and RVFWT, right ventricular free wall thickness.